Earth and Planetary Science Letters 620 (2023) 118349

Contents lists available at ScienceDirect

Earth and Planetary Science Letters

journal homepage: www.elsevier.com/locate/epsl

# Crystal plasticity and fluid availability govern the ability of titanite to record the age of deformation

Stefania Corvò [a,b,*], Matteo Maino [a,b], Sandra Piazolo [c], Andrew R.C. Kylander-Clark [d], Andrea Orlando [e], Silvio Seno [a], Antonio Langone [a,b,*]

[a] Department of Earth and Environmental Sciences, University of Pavia, Pavia, Italy
[b] Institute of Geosciences and Earth Resources of Pavia, C.N.R., Pavia, Italy
[c] School of Earth and Environment, University of Leeds, Leeds, United Kingdom
[d] Department of Earth Science, University of California, Santa Barbara, United States
[e] Institute of Geosciences and Earth Resources of Florence, C.N.R., Firenze, Italy

ARTICLE INFO

*Article history:*
Received 27 December 2022
Received in revised form 28 July 2023
Accepted 4 August 2023
Available online xxxx
Editor: A. Webb

*Keywords:*
titanite
mylonites
shear zone
microstructure
petrochronology
fluid-mineral interactions

ABSTRACT

Here, we study the relationships of titanite-hosting microdomains, intragrain chemical variations, microstructure and fluids with the aim of deciphering the reliability of titanite U–Pb dating to constrain the age of deformation in mylonitic rocks. We investigate these relationships in a post-Variscan amphibolite-facies shear zone developed in the mid-low continental crust (Ivrea-Verbano Zone, Southern Alps, Italy). Quantitative orientation analyses along with textural imaging of titanite are combined with trace-element analyses and U–Pb age dating. Titanite is studied in mm- to cm-scale layered rocks showing compositional variation consisting of alternating 'amphibole-rich' (i.e., amphibolites) and 'clinopyroxene/plagioclase-rich' domains (i.e., calc-silicates). Titanite from amphibole-rich domains shows predominance of crystal–plastic deformation features, as abrupt or progressive core-to-rim structures characterized by increasing lattice distortion and local dislocation density, associated with the development of abundant subgrains and rare newly nucleated grains. We suggest that these microstructures form while interacting with small amounts of fluids circulating along the grain boundaries. Consequently, locally the chemistry of titanite is changing. In the clinopyroxene/plagioclase-rich domains, titanite is mostly undeformed and rarely shows bending localized in discontinuous narrow rims/tips. In these domains, fluid-mediated replacement reactions are either rare or absent, as also indicated by weak chemical variations across and among grains. These observations suggest different reactivities with respect to the same P-T-fluid conditions of the two compositional domains, which coexist within the same sample at the thin section scale. U–Pb data show correlations with chemical and microstructural domains that differ as function of the composition of the microdomain. This correlation is more apparent within amphibole-rich domains where microstructures characterized by high lattice distortion/dislocations and/or subgrains show significant variations of REE, Zr, Y, Nb, U with respect to the low deformed portion of grains. These titanite domains define an isotopic population providing the youngest (Jurassic) lower intercept age. A less clear correlation between titanite chemistry and microstructures is observed in clinopyroxene/plagioclase-rich domains. Here, the rare titanites showing lattice distortion and minor Sr depletion define a population providing a similar Jurassic lower intercept age. Therefore, our results demonstrate that microstructurally and chemical calibrated U–Pb dating of titanite provides realistic ages of shear zone activity, only in case of predominance of crystal-plastic processes and of local interaction of titanite with small amounts of fluids focused along grain boundaries. Finally, the different footprints recorded by titanite grains strongly depend on the composition of cm- or mm-scale interlayered domains in which titanite occurs.



## 1. Introduction

The age at which deformation localizes into shear zones is key information needed to constrain timing and approximate duration of the sequence of events associated with crustal processes such

* Corresponding authors.
*E-mail addresses:* stefania.corvo@unipv.it (S. Corvò), antonio.langone@unipv.it (A. Langone).

https://doi.org/10.1016/j.epsl.2023.118349

as rifting or mountain building. In-situ isotopic data from accessory minerals – such as zircon, monazite, titanite and rutile - have been largely used to link ages with pressure-temperature (P-T) conditions, metamorphic reactions and petrologic evolution (e.g., Cherniak, 2010; Kohn, 2017; McGregor et al., 2021). It has been recently shown how crystal-plastic deformation may enhance element mobility and promote isotopic system perturbation within these accessory minerals, potentially providing direct constrains on the timing of deformation (e.g., Piazolo et al., 2012, 2016; Erickson et al., 2015; Smye et al., 2018; Moore et al., 2020; Moser et al., 2022). Moreover, the circulation of fluids can be recorded by the geochronometers in response to fluid-mediated replacement reactions (e.g., Coupled Dissolution Precipitation - CDP; Rubatto and Hermann, 2003; Putnis, 2009; Varga et al., 2020; Gordon et al., 2021; Moser et al., 2022).

In the last decade, titanite ($CaTiSiO_5$) has gained popularity in the petrological community due to its advantageous compositional and textural properties that make it an important tracer of fluids and reactions in the Earth's continental crust (e.g., Oberti et al., 1981; Kohn, 2017). Titanite is a widespread accessory mineral that crystallizes over a wide range of crustal pressures and temperatures in many rock types, including metamorphosed mafic rocks, calc-silicates as well as felsic calc-alkaline igneous rocks (e.g., Frost et al., 2000; Hayden et al., 2008; Kohn, 2017). Titanite incorporates a wide range of minor and trace elements, including significant concentrations of uranium, rare-earth elements (REE) and high-field-strength elements (HFSE) making it a robust petrochronometer (e.g., Frost et al., 2000; Kohn, 2017; Garber et al., 2017; Mottram et al., 2019; Scibiorski et al., 2019; Scibiorski and Cawood, 2022). Its use as a petrochronometer is potentially hampered as its composition and modal abundance are strongly influenced by the bulk-rock chemistry especially in high-grade metamorphic rocks (e.g., Scott and St-Onge, 1995; Kohn, 2017; Scibiorski et al., 2019; Scibiorski and Cawood, 2022). Since titanite is involved in number of metamorphic reactions of major rock forming minerals (e.g., Frost et al., 2000), it can be potentially useful to constrain the timing of these reactions developed at specific P-T conditions.

Titanite U–Pb ages are traditionally interpreted as susceptible to diffusive resetting (Cherniak, 1993), although Pb lattice diffusion in an intact crystal at $T \leq 750\,^{\circ}C$ is negligible (Kohn and Corrie, 2011; Stearns et al., 2015; Holder and Hacker, 2019). Recent studies have revealed potential decoupling between the U–Pb isotopic system and the behavior of trace-elements (e.g., Y, Zr, REE) as P-T conditions change through time (Garber et al., 2017). Furthermore, titanite is prone to recrystallize dynamically and statically (Spencer et al., 2013; Stearns et al., 2015; Kirkland et al., 2016) resulting in significant Pb diffusion, compositional zoning, variations in trace-element content and destruction or partial preservation of earlier microstructural features (Cherniak, 1993; Gordon et al., 2021; Bonamici and Blum, 2020; Moser et al., 2022). Similar to zircon (e.g., Piazolo et al., 2012), crystal-plastic deformation-induced microstructures, such as subgrains, can be dated, therefore providing potential ways to directly constrain the timing of deformation (e.g., Erickson et al., 2015; Moser et al., 2022). Titanite that experienced a multi-stage tectono-metamorphic event may contain multiple generations of grains/domains likely showing complex chemical/deformation and U–Pb patterns (Frost et al., 2000; Stearns et al., 2015; Scibiorski and Cawood, 2022). However, in-depth understanding of links between fluid, reactions and deformation may offer the opportunity to date deformation directly. Titanite U–Pb data can only be interpreted if the interplay between growth, syntectonic and post-tectonic modification is established since the measured isotopic composition may reflect the grain growth or the subsequent processes (cooling or fluid- and deformation-driven reorganization of the crystal lattice). Hence, to interpret titanite age data it is highly recommended to frame titanite at the grain-scale context and with respect to the chemical composition of the rock microdomains (Bestmann et al., 2005; Kohn and Corrie, 2011; Kirkland et al., 2016; Garber et al., 2017; Scibiorski et al., 2019; Cavosie et al., 2022).

In this contribution, we study titanite grains collected from mylonites with the aim of testing whether titanite petrochronology can be used to date deformation. We choose to study the Anzola shear zone, which is a major extensional structure affecting the Variscan mid-low continental crust of the Ivrea-Verbano Zone (Southern Alps; Fig. 1). Although its metamorphic evolution has been well established (Corvò et al., 2022), the age of deformation is still poorly constrained. We selected two different compositional domains interlayered at the mm- to cm-scale, which have experienced the same regional P-T conditions and deformation history. Our results show that titanite has different composition as function of the hosting microdomains and that it develops different textural and microstructural patterns as a function of the reactivity of host rock mineral assemblage.

In particular, a significant coupling between microstructures (high lattice distortions and development of subgrains) with chemical/isotopic data is apparent in amphibole-dominated microdomains. Titanite petrochronology and microstructures allow to constrain the activity of the Anzola shear zone at lower Jurassic time, resulting one of the major structures active during the Alpine Tethyan rifting.

## 2. The Ivrea-Verbano Zone and the Anzola shear zone

The Anzola shear zone crops out in Val d'Ossola, north-western Italy, where the Ivrea-Verbano Zone (IVZ) displays one of the best-preserved cross sections through the middle-low continental crust of the fossil passive margin of the Southern Alpine basement (Fig. 1; Corvò et al., 2022 and references therein). The IVZ consists of a pre-Variscan volcano-sedimentary metamorphic sequence (Kinzigite Formation) comprising metapelites, amphibolite and marbles overlying gabbros, diorites and minor peridotitic bodies (Mafic Complex; Fig. 1A; Zingg, 1990; Klötzli et al., 2014; Kunz et al., 2014). Mantle-derived mafic magmatism started in the Carboniferous (~314 Ma; Klötzli et al., 2014), mainly developed during the early Permian (290-270 Ma; Peressini et al., 2007) and locally occurred later from late Permian to Jurassic (Zanetti et al., 2013; Locmelis et al., 2016; Denyszyn et al., 2018). At a regional scale, peak metamorphic conditions decrease from granulite (~900 °C; 0.9 GPa) to amphibolite facies (~600 °C; ~0.4 GPa) from NW to SE (Zingg, 1990; Redler et al., 2012; Kunz et al., 2014). High temperature metamorphic conditions persisted over a large time span from Late Carboniferous (~316 Ma) to the Early Permian (Ewing et al., 2013; Kunz et al., 2018; Williams et al., 2022).

The spatially progressive switch from granulite to amphibolite facies is marked by a transition zone characterized by abundant migmatites (e.g., Redler et al., 2012; Kunz et al., 2014) that were involved in several high-temperature (granulite-amphibolite facies) mylonites, including the Anzola shear zone (Fig. 1; e.g., Rutter et al., 2007; Corvò et al., 2022; Simonetti et al., 2023). These structures are thought to have accommodated, since the Triassic, crustal thinning in the mid-lower continental crust during the early Tethyan rifting (Fig. 1B, e.g., Beltrando et al., 2015; Petri et al., 2019 and reference therein). In particular, the Anzola sheared rocks are interpreted as mylonites and ultramylonites developed in a multi-lithological sequence made of alternating amphibolites, paragneisses and calc-silicates (Fig. 1C, see Fig. 12 from Corvò et al., 2022 for a complete description). Mylonitic deformation started at high temperature (~820 °C; 0.8 GPa) with presence of melt and continued as solid-state deformation down to amphibolite facies (~650 °C; 0.7 GPa; Corvò et al., 2022). Syn-rift deformation was also recorded in the upper crust as documented by brittle-ductile

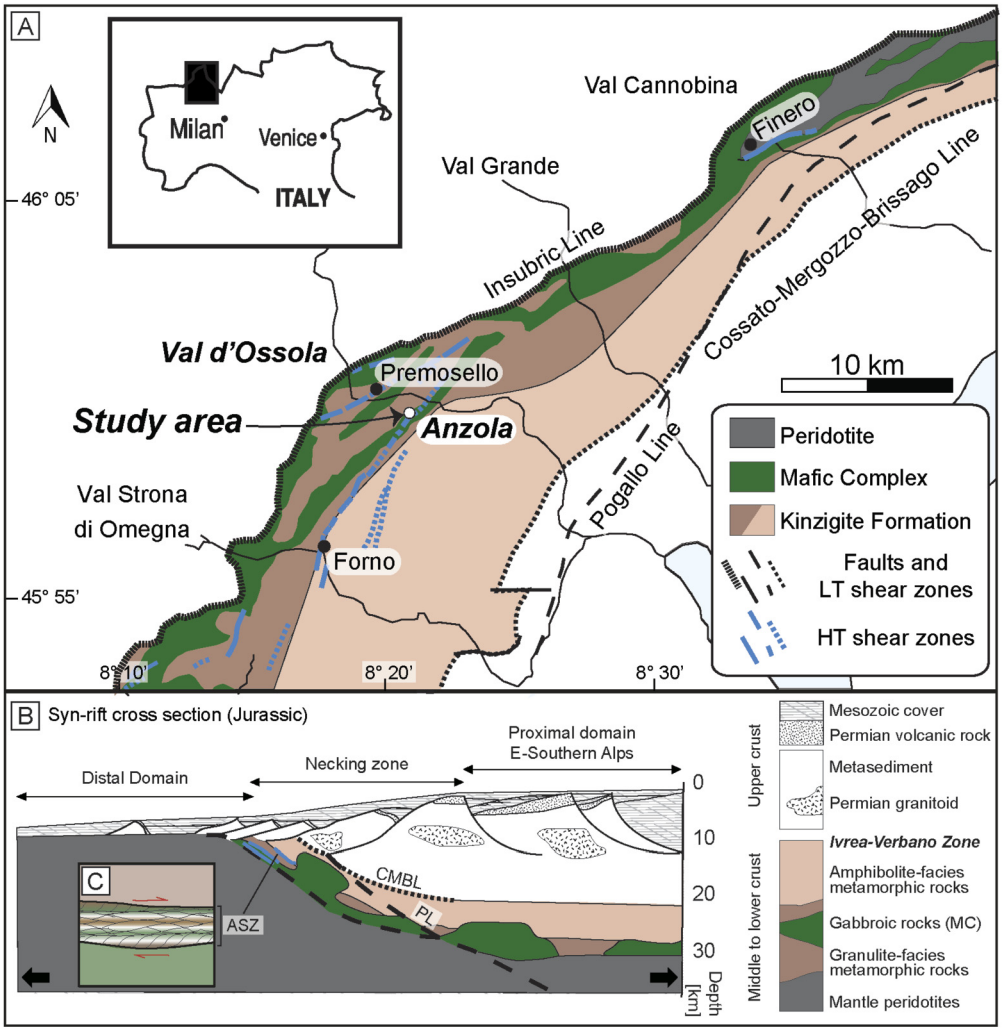


**Fig. 1.** Geological sketch map of: A) the Ivrea-Verbano Zone (IVZ), modified after Corvò et al. (2022). B) Reconstructed post-rift cross-section and relative lithotectonic map modified after Beltrando et al. (2015); Petri et al. (2019). C) Sketch of the Anzola shear zone showing alternated mylonitic banded amphibolites and calc-silicate in contact with gabbroic rock and granulite-facies metasediments (modified after Corvò et al., 2022). The red arrows show the kinematics and the sense of shear of the shear zone referring to the syn-rifting evolution during Jurassic time. KF: Kinzigite Formation; MC: Mafic Complex; PL: Pogallo Line; CMBL: Cossato-Mergozzo-Brissago Line; ASZ: Anzola Shear Zone; LT: Low Temperature; HT: High Temperature.

shear zones and faults (e.g., the Pogallo Line, PL, Mulch et al., 2002; Fig. 1A, B).

Although there is a general agreement on a Late Triassic to Early Jurassic age for the shear zones developed in the IVZ (e.g., Petri et al., 2019 and references therein), there are a few timing constraints concerning their evolution (see Simonetti et al., 2021 for a complete review). The most reliable dating has been provided for the Pogallo Line developed in upper crustal levels (green-schist facies), which is constrained between 210 and 170 Ma ($^{40}Ar/^{39}Ar$ on muscovite, Rb-Sr on biotite and K-Ar on micas; Zingg, 1990; Mulch et al., 2002; Wolff et al., 2012). Evidence for Triassic–Jurassic high-temperature deformation has been recently documented also for other shear zones exposed in Val d'Ossola (e.g., Kusiak et al., 2019) and Val Cannobina (e.g., Boriani and Villa, 1997; Langone et al., 2018; Corvò et al., 2020; Fig. 1A). However, the Anzola shear zone lacks extensive geochronological investigations. Brodie et al. (1989) performed the only attempt to date the activity of the amphibolite-facies mylonites through $^{40}Ar/^{39}Ar$ dating of hornblende. They reported a minimum age of ~247 Ma for unsheared mafic rocks and ~210-215 Ma for syn-kinematic amphibole grains. The authors suggested that extension in the Ivrea-Verbano lower crust initiated prior to 280 Ma, probably around 300 Ma, and began a period of crustal thinning and cooling of more than 100 Myr duration.

## 3. Sample selection and analytical strategy

Two titanite-bearing thin sections (i.e., AN01A, AN01D) from mylonites (sample AN01; Fig. 2A) of the Anzola shear zone were selected for *in-situ* titanite petrochronological analyses. The selected thin sections are representative for the variability in mineral phases and phase modes within the studied mylonites (Fig. 2A). AN01A was chosen to represent the amphibole-rich domains (Amph-rich, hereafter; Fig. 2B, D), since it is mostly made by amphibole (52 vol.%) + plagioclase (29 vol.%) + clinopyroxene (diopside, 14 vol.%) + titanite (5 vol.%), while AN01D is representative of the clinopyroxene/plagioclase-rich domains (hereafter Cpx/Pl-rich; Fig. 2C, E) being mostly composed of plagioclase (52 vol.%) + clinopyroxene (hedenbergite, 28 vol.%) + garnet (9 vol.%) + amphibole (6 vol.%) + titanite (5 vol.%). These domains alternate at both the mm- and cm-scale where especially the Cpx/Pl-rich domains form discontinuous, variably thick bands showing boudinage (cf. Fig. 2A white arrows). Detailed petrographical and microstructural descriptions of the studied mylonites are provided in Corvò et al. (2022).

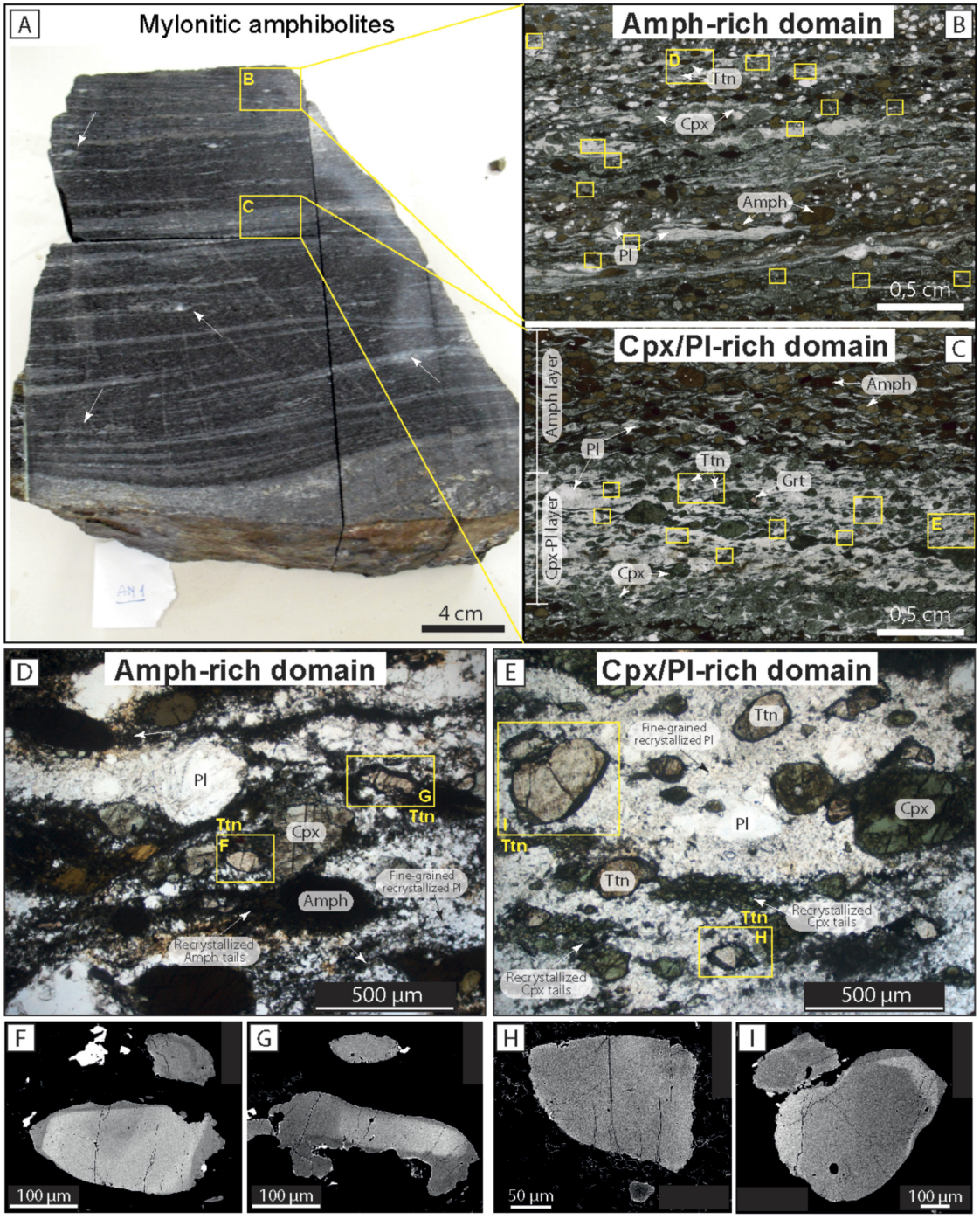


**Fig. 2.** Petrographical and textural features of the studied titanite-bearing mylonites. A) Hand specimen (30x50 cm) of the studied banded mylonites. In yellow boxes are highlighted the microdomains (B: Amph-rich; C: Cpx/Pl-rich) selected for titanite *in-situ* analyses and representative of the main textural microdomain features. White arrows highlight Cpx/Pl-rich parts that show boudinages. B, C) Plane polarized (PPL) photomicrographs of mylonites for: B) Amph-rich domains and C) Cpx/Pl-rich domains. Note that amphibole is shades of dark brown, whereas the cpx is shades of green. Small yellow boxes show locations of titanite grains (light brown) outlining their textural distribution in the microdomain. D, E) Representative PPL photomicrographs showing the mineral assemblages and textures of main mineral phases and titanite grains for Amph-rich and Cpx/Pl-rich domains, respectively. White and black arrows highlight dynamic recrystallization features. F, G) Back-Scattered Electron (BSE) images highlighting the zoning from core to rim in titanites from the Amph-rich domains. H, I). BSE images of different zoning within titanite grains from the Cpx/Pl-rich domains.

Titanite grains were identified and characterized firstly by Back-Scattered Electron images (BSE) and then analyzed for quantitative orientation data by Electron Backscatter Diffraction analysis (EBSD) to determine textural and microstructural features. Titanite quantitative chemical analyses (major, minor and trace elements: $SiO_2$, $TiO_2$, $Al_2O_3$, FeO, MnO, CaO, $Y_2O_3$, $La_2O_3$, $Nb_2O_5$, $Ce_2O_3$, $Nd_2O_3$, F) and X-ray maps (Si, Ti, Al, Ca, Fe, F, Zr, Nb, La, Ce, Nd) were determined by Electron Probe Microanalyzer (EPMA). This was followed by Laser-Ablation Split-Stream Inductively Coupled Plasma Mass Spectrometer (LASS-ICP-MS) analyses to determine the isotopic date and trace-element concentrations. For further details about data acquisition and treatment see Appendix A. Supplementary Material Methods section. Mineral abbreviations follow Whitney and Evans (2010).

## 4. Results

### 4.1. Petrography of mylonites

Titanite-bearing mylonites from the Anzola shear zone consist of mm- to cm-scale alternating amphibolites (greenish darker layers, Amph-rich domains; Fig. 2) and calc-silicates (whitish layers; Cpx/Pl-rich domains; Fig. 2; Corvò et al., 2022). Cpx/Pl-rich domains generally occur as boudins surrounded by Amph-rich domains, suggesting that these parts are rheologically harder than Amph-rich ones (Fig. 2A). The mylonitic fabric is characterized by porphyroclasts (diameter of 0.5-1.0 mm) of plagioclase, amphibole or clinopyroxene (Fig. 2B, C). Garnet occurs as fragmented porphyroclasts within the Cpx/Pl-rich domains (Fig. 2C). Porphyroclasts are surrounded by a fine-grained matrix consisting of plagioclase + clinopyroxene + titanite ± amphibole ± garnet ± epidote ± calcite (Table S1). Small grains of amphibole constitute 'recrystallization tails' next to amphibole porphyroclasts within Amph-rich domains, whereas they are rare in the matrix of Cpx/Pl-rich domains (Fig. 2D, E). Syn-kinematic biotite and calcite occur rarely along the fine-grained recrystallized matrix at the amphibole and clinopyroxene porphyroclast tails, respectively. Titanite, ilmenite, apatite and zircon are the common accessory minerals (Table S1). Titanite is preferentially dispersed in the matrix (Fig. 2B-E), but also forms inclusions in amphibole and clinopyroxene porphyroclasts. Quite abundant ilmenite (~2%) occurs as interstitial grains along the foliation, bordering titanite grains and/or locally forming discontinuous ~25 μm thick rims around titanite (Figs. 2F, G; S3). Late alteration mineral phases such as calcite, epidote, chlorite and white mica fill fractures and veins crosscutting the foliation or partially replace the primary mineral assemblage (Fig. S1).

### 4.2. Titanite textural and microstructural features

#### 4.2.1. Titanite in amphibole-rich domains

In Amph-rich domains, titanites are mainly located at contacts with or close to porphyroclasts or within the fine-grained matrix itself (Figs. 2B, D; 3Ai-Gi). Titanite predominantly shows elongated and sigmoidal shapes, while grains with a euhedral wedge shape are less common (Figs. 2D, F, G; S2). Grain size ranges between ~100 × 300 μm and ~250 × 500 μm (Figs. 2D, F, G; S2; Table S1). Grain boundaries locally show angular cusps with lobate edges (Figs. 2D, F, G; S2). Almost all titanite grains (80%) display lighter core to darker rim zoning in BSE images with rims marked by straight boundaries towards the core typically <50 μm in width (Figs. 2F, G; S2C, D). Aligned pore trails and microfractures may be observed towards the rims (Fig. S2E, F). Subhedral/anhedral ilmenite is locally found at the rims of titanite (Figs. 2F; 3Aii-Eii; S3).

Twenty-three titanites from Amph-rich domains were analyzed by EBSD (Fig. 3). Some of them contain a set of polysynthetic twin lamellae (Fig. 3Aiii, Ciii, Fiii). These sets occur as 0.5 μm wide straight to slightly kinked twins, which cross the grain and terminate against grain boundaries with a disorientation from the host grain by ~74°/<102>, similar to twins documented in previous studies (Fig. 3Ciii-v; Timms et al., 2019; McGregor et al., 2021).

Based on their microstructural features, titanites are subdivided into three different types (T): T1) domains without significant lattice distortions (<6°; four grains; Fig. 3A); T2) titanites with distortions focused only at the rim/tips (ten grains; Fig. 3B, C); T3) grains with significant intracrystalline lattice distortion reaching up to ~30° across the whole grain including planar deformation bands, continuous and discontinuous lattice distortions from core to rim (continuous; six grains; Fig. 3D, E; discontinuous; three grains; Fig. 3F, G). Some of T2 grains develop subgrains close to their grain boundaries (Fig. 3Biii-v, Ciii-v), whereas some exceptional grain aggregates of T3 exhibit domains with distinctly different orientation and low internal dislocation density (Fig. 3F, G). These last grains are termed "newly nucleated grains" due to their distinct crystallographic orientations; they are easily recognizable by the random orientation changes shown in the pole figures (Fig. 3Fiv-v; Giv-v). Except for T1, most grains preserve domains with variable degree of lattice distortions averaging at ~15° across individual grain (Fig. 3; Table S1).

Quantification of the local dislocation density (measured as Weighted Burgers vector, hereafter WBV) for T2 and T3 grains provides an average value for laser spot analyses of 0.0014 $\mu m^{-1}$ (Table S1; see Appendix A.1 for further details in WBV calculation). Systematic distortion patterns in pole figures show that T1 and T2 grains deformed by crystal-plastic deformation with one or two main slip systems activated. Here, a prevalence of the slip system (001) [100] is seen (Fig. 3A-Eiv-vi). T3 grains exhibit planar deformation bands (PDBs; McGregor et al., 2021) with systematic crystallographic misorientation corresponding to a slip plane of (111) and slip direction of <110> (and equivalent (-11-1), <-110>, as defined by using pole figures; Fig. 3Diii, Eiii).

#### 4.2.2. Titanite in clinopyroxene/plagioclase-rich domains

In Cpx/Pl-rich domains, titanites are generally surrounded by fine-grained recrystallized plagioclase (Figs. 2C, E; 4Ai-Gi), and some grains are close to or in contact with clinopyroxene porphyroclasts (Figs. 2C, E; 4Ai-Gi). Titanite may be either: i) small (~100 × 250 μm) elongated/sigmoidal in shape with irregular grain boundaries and lobated rims, or, ii) large (~250 × 500 μm) wedge-shaped (Figs. 2E, H, I; S3; Table S1). Grains mostly do not show an apparent internal zoning in BSE images (Figs. 2H; S3). Rarely, a faint patchy core-rim zoning (Fig. 2I) or narrow (<10 μm) lighter rims surrounding darker cores are seen (Figs. 2H; S3F).

Three microstructure types are distinguished: T1) titanite without or with very little lattice distortion (twenty grains; Fig. 4Aiii); T2) with lattice distortions focused only to the rim/tips (up to 15°; five grains; Fig. 4Bii, Cii, Diii); T3) domains with internal distortions throughout whole grains (five grains; Fig. 4Eii-Giii). Few T2-T3 grains develop distinct subgrains (Fig. 4Biii-v, Fiii-v), however in rare cases tiny "newly nucleated grains", i.e., grains with a distinct orientation, are seen close to T3 grains (Fig. 4Ciii-iv, Giii-v).

Compared to titanite from Amph-rich domains, for Cpx/Pl-rich domains WBV analyses show a lower average local dislocations density (0.0001 $\mu m^{-1}$, Table S1). Despite apparent similarities with the distorted grains of the Amph-rich domains, Cpx/Pl-rich titanites show a prevalence of a random distribution of lattice distortions in pole figures (Fig. 4Civ-v; Giv-v) and only rarely clear systematic lattice distortions related to crystal plasticity (Fig. 4Aiv-v; Div-v). Similar to titanites in Amph-rich domains some titanites contain a set of polysynthetic twin lamellae which are mostly straight to locally slightly kinked or/and tapered (five grains; ~74°/<102>; Fig. 4Cii, Eii; Giii).

### 4.3. Titanite chemical composition

The major, minor and trace elements distribution reveal both titanite internal zoning and chemical variations between individual titanite grains from the two compositional domains (Amph-rich vs. Cpx/Pl-rich). Combining the BSE-images with quantitative chemical analyses and X-ray maps, core to rim zoning is recognizable (Figs. 5, S4; Table S1).

In Amph-rich domains, seventeen titanite grains were analyzed. The BSE-brighter cores are characterized by slightly lower CaO content with respect to rim (27.6 ± 0.3 → 28 ± 0.4 wt.%). $SiO_2$ (30.1 ± 0.2 → 30.3 ± 0.2 wt.%) and $TiO_2$ (37.4 ± 0.4 → 37.7 ± 0.5 wt.%) show locally a similar trend (Fig. 5C). Conversely, the BSE-brighter

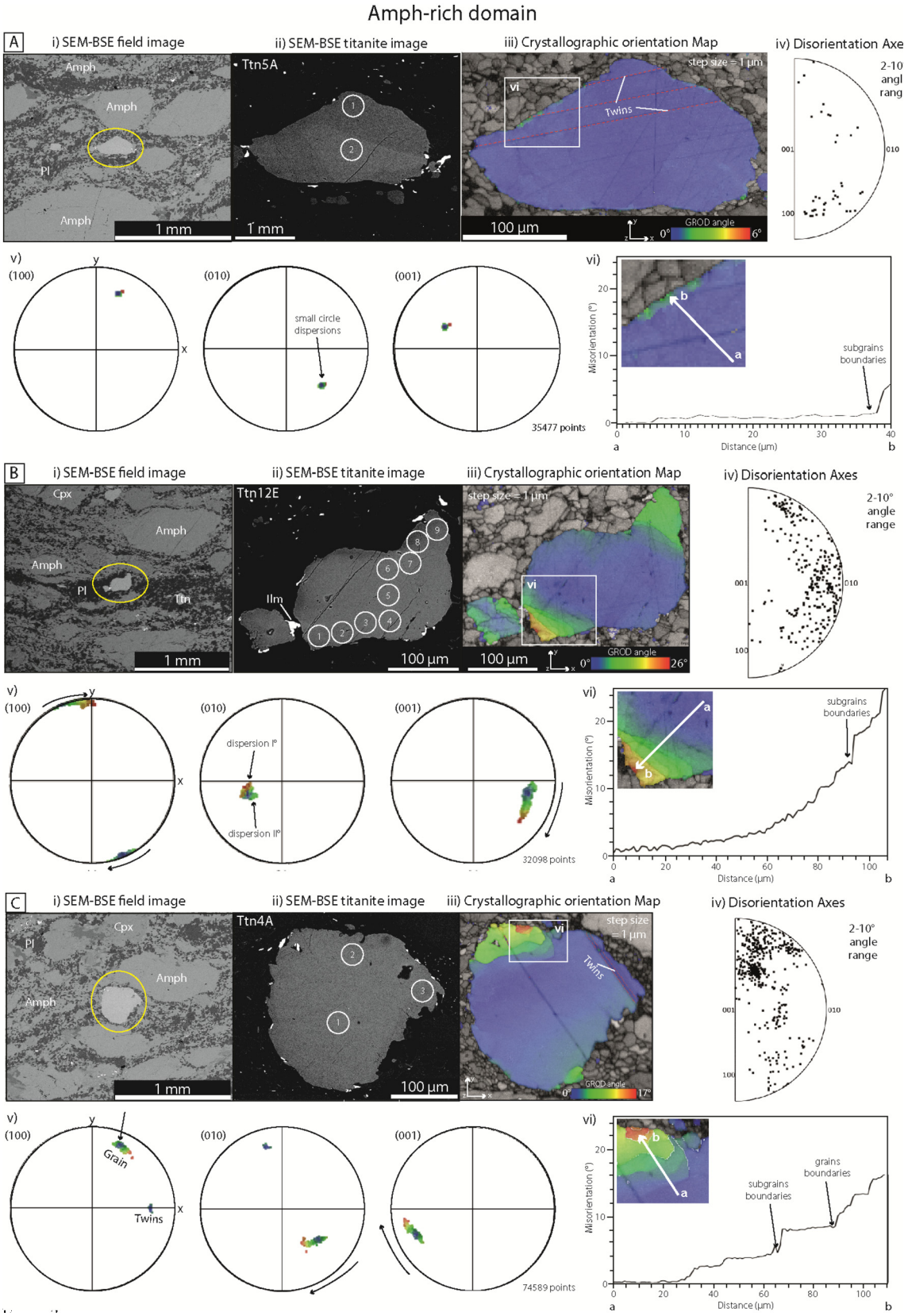


**Fig. 3.** Representative textural and microstructural features of the different three types (T) distinguished for titanite grains from the Amph-rich domains. A) titanite with no lattice distortions within the whole grain (microstructural type T1); B, C) grains with distortions focused only to the rim/tips (T2); D, E) titanite with planar deformation bands and internal distortions with a continuous core to rim trend; F, G) grains with low internal dislocation density and distortion up to ~30° developing newly nucleated grains (T3). i-ii) BSE panoramic images of analyzed titanite grain location, textural zoning and features. The numbered white circles in ii) represent the LASS spot analyses performed on titanite grains numbered according to the U–Pb analyses reported in Tables S1. iii) Relative crystallographic orientation map (GROD angle map) highlight degrees of distortion across the grain and when presented the sets of twins. iv) Distribution of the disorientation axes data across the grain plotted in pole figures shown in iii). v) Pole figures for (100), (010), (001) showing the orientation of grain, subgrains, twins and newly nucleated grains. Lower hemisphere, equal area projections in the sample x-y-z reference frame. The colors of point in pole figures reflect the colors of the GROD angle map for titanite in iii). Black arrows highlight the way of dispersions. vi) Misorientation profile (a-b) across the grain area from the box in iii. PDB = planar deformation band.

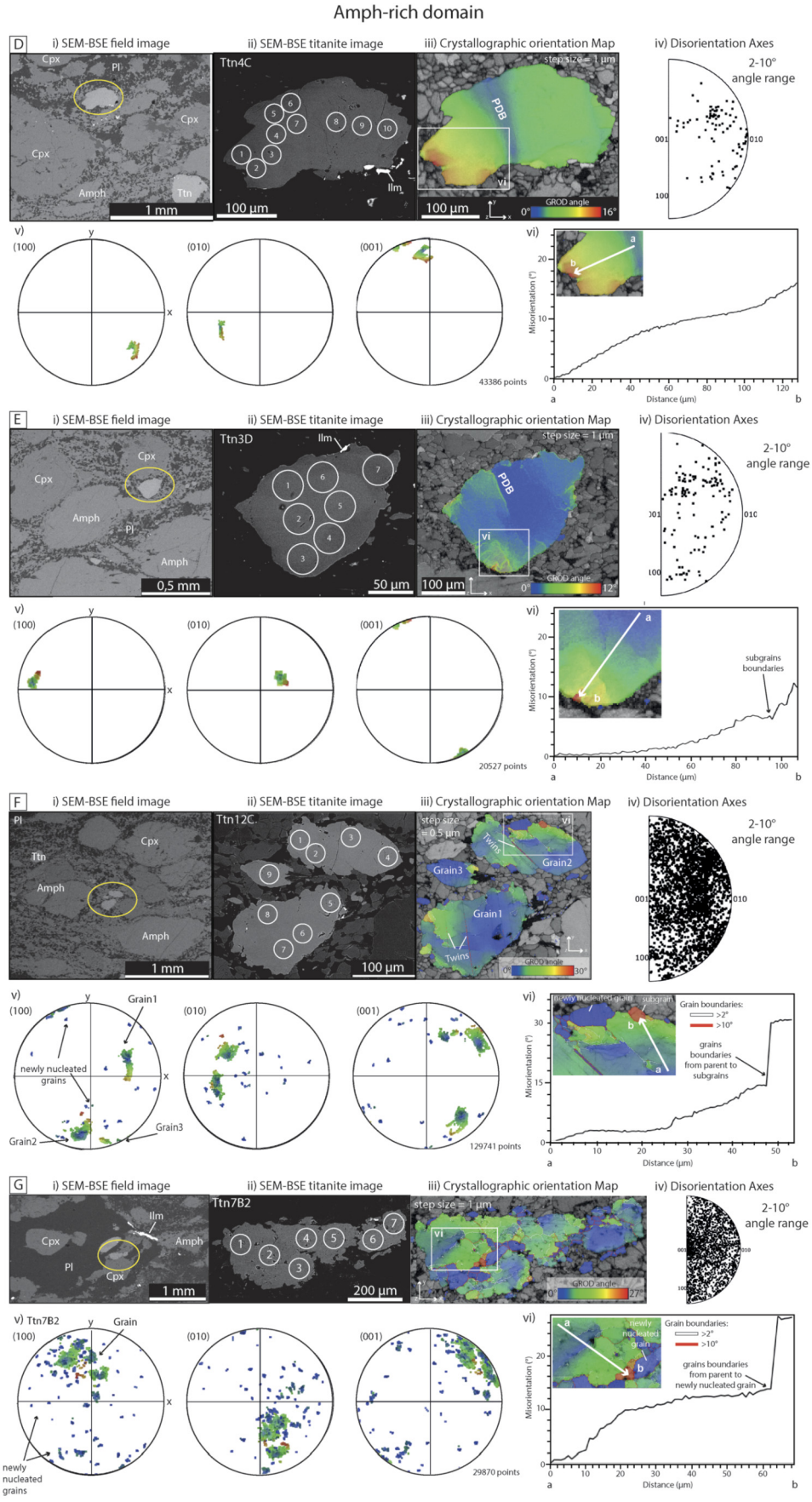


**Fig. 3.** (*continued*)

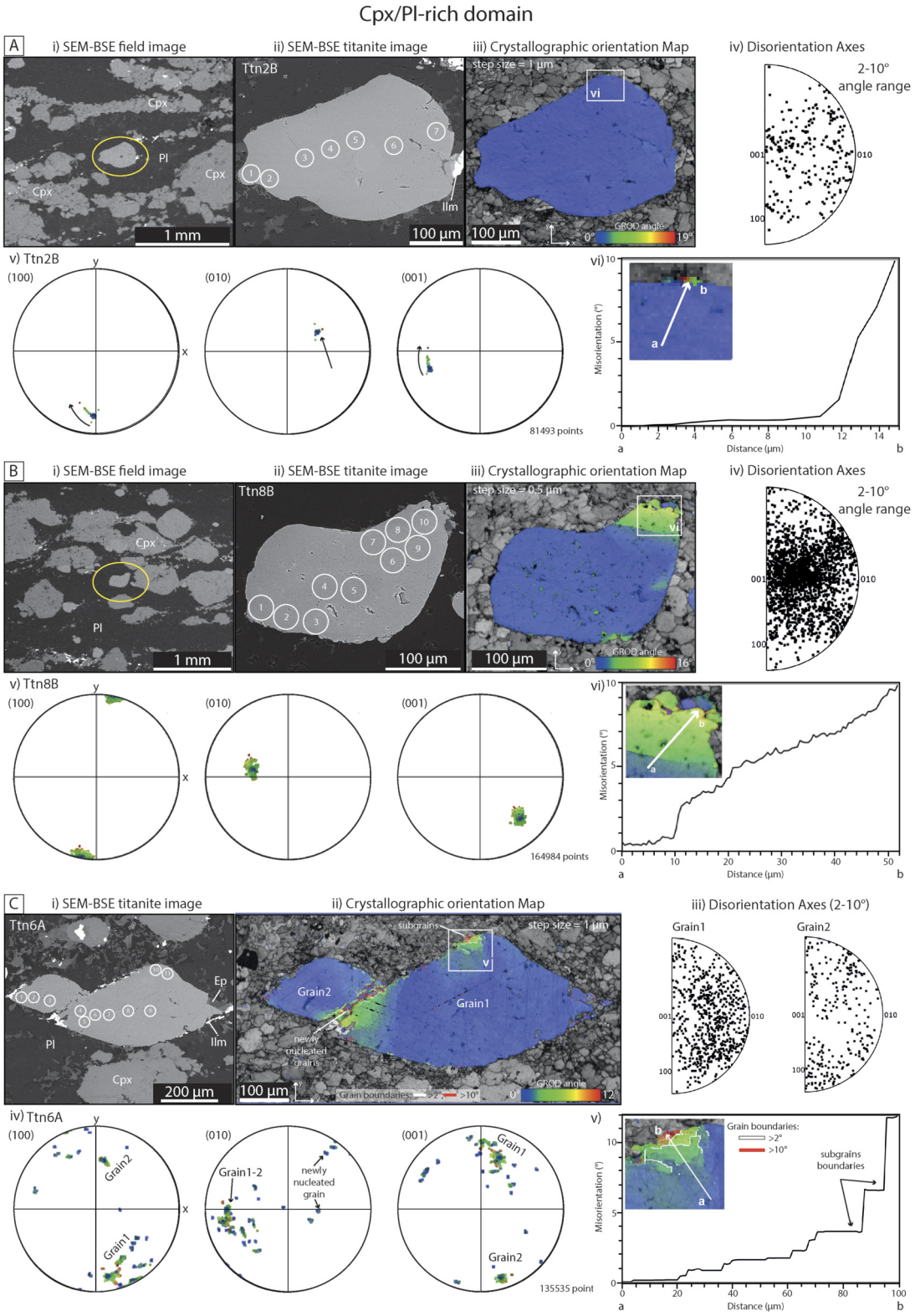


**Fig. 4.** Representative textural and microstructural features of the different three types (T) distinguished for titanite grains from the Cpx/Pl-rich domains. A) titanite with no lattice distortions within the whole grain (T1); B, C) grains with distortions focused only on the rim/tips and locally associated with subgrains (T2); D-G) titanite with internal distortions (and planar deformation bands) increasing from core to rims (T3). i-ii) BSE panoramic images of analyzed titanite grain location, textural zoning and features. The numbered white circles in ii) represent the LASS spot analyses performed on titanite grains numbered according to the U–Pb analyses reported in Tables S1. iii) Relative crystallographic orientation map (GROD angle map) showing degrees of distortion across the grain and when presented the sets of twins. iv) Distribution of the disorientation axes data across the grain plotted in pole figures shown in iii). v) Pole figures for (100), (010), (001) showing the orientation of grain, subgrains and twins. Note likely rotation of recrystallized grains as indicated by an arrow in (Av). Lower hemisphere, equal area projections in the sample x-y-z reference frame. The colors of point in pole figures reflect the colors of the GROD angle map for titanite in iii). Black arrows highlight the way of dispersions. vi) Misorientation profile (a-b) across the grain area from the box in iii. PDB = planar deformation band.

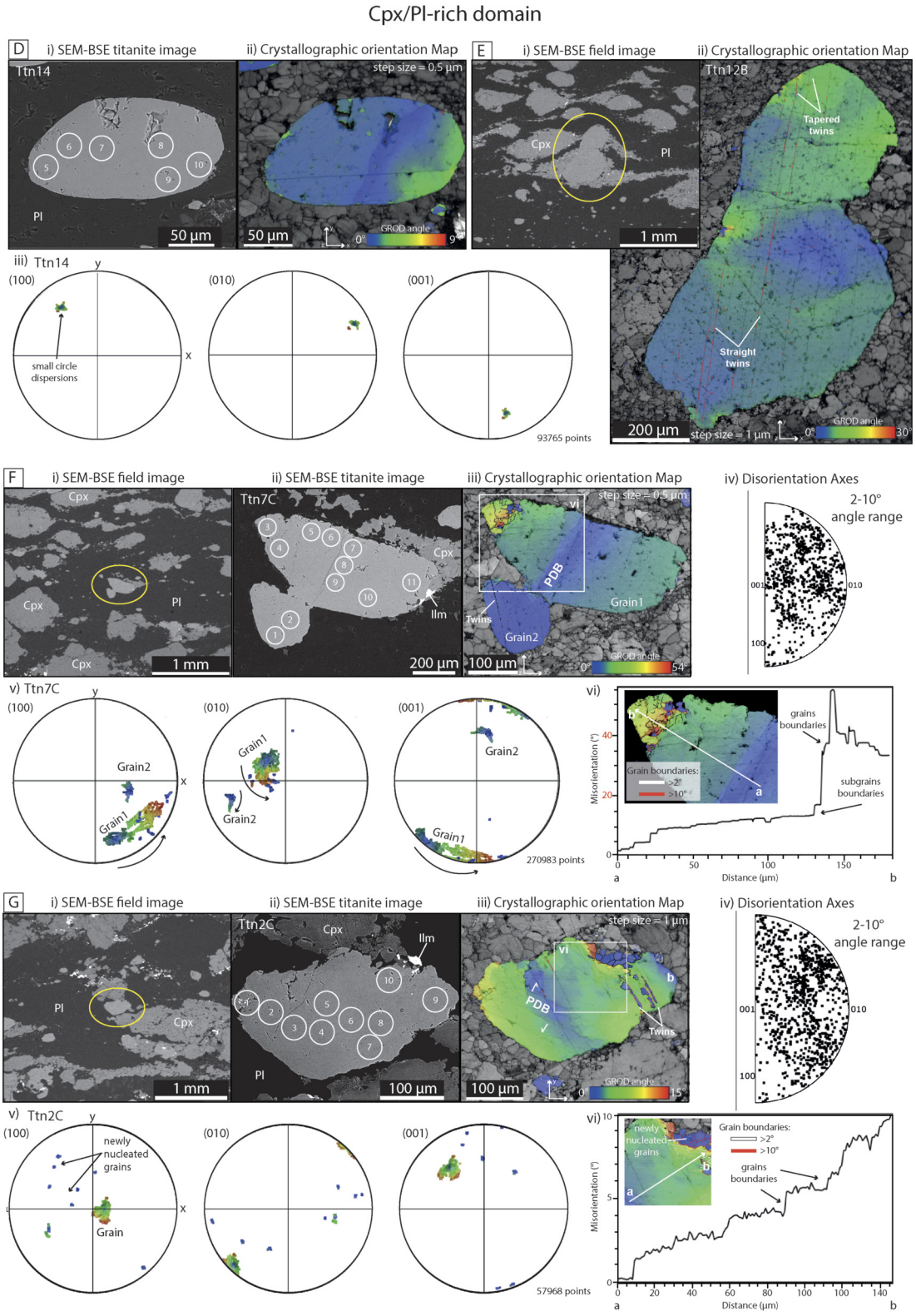


**Fig. 4.** (*continued*)

cores show higher $Al_2O_3$, $Ce_2O_3$, $Nd_2O_3$ and $ZrO_2$ contents with respect to rims (1.6 ± 0.1 → 1.5 ± 0.2 wt.%, 0.48 ± 0.11 → 0.35 ± 0.13 wt.%, 0.24 ± 0.08 → 0.20 ± 0.08 wt.%, 0.15 ± 0.03 → 0.08 ± 0.03 wt.%, respectively; Fig. 5D-F).

In the Cpx/Pl-rich domains, twelve titanite grains were analyzed. Among these, nine lack any marked zoning on the BSE images (Figs. 2H, 5B; S3A-E; S4), whereas three grains have a weak BSE-zoning with darker core to brighter rim (Figs. 2I, S4C, D). All the grains show a slight decrease of CaO (28.4 ± 0.4 → 28.3 ± 0.4 wt.%), $SiO_2$ (30.2 ± 0.3 → 30.2 ± 0.2 wt.%), $TiO_2$ (38.1 ± 0.4 → 38.2 ± 0.2 wt.%) and $ZrO_2$ (0.16 ± 0.04 → 0.10 ± 0.08 wt.%) from core to rim and an opposite trend for $Al_2O_3$ (1.2 ± 0.1 → 1.3

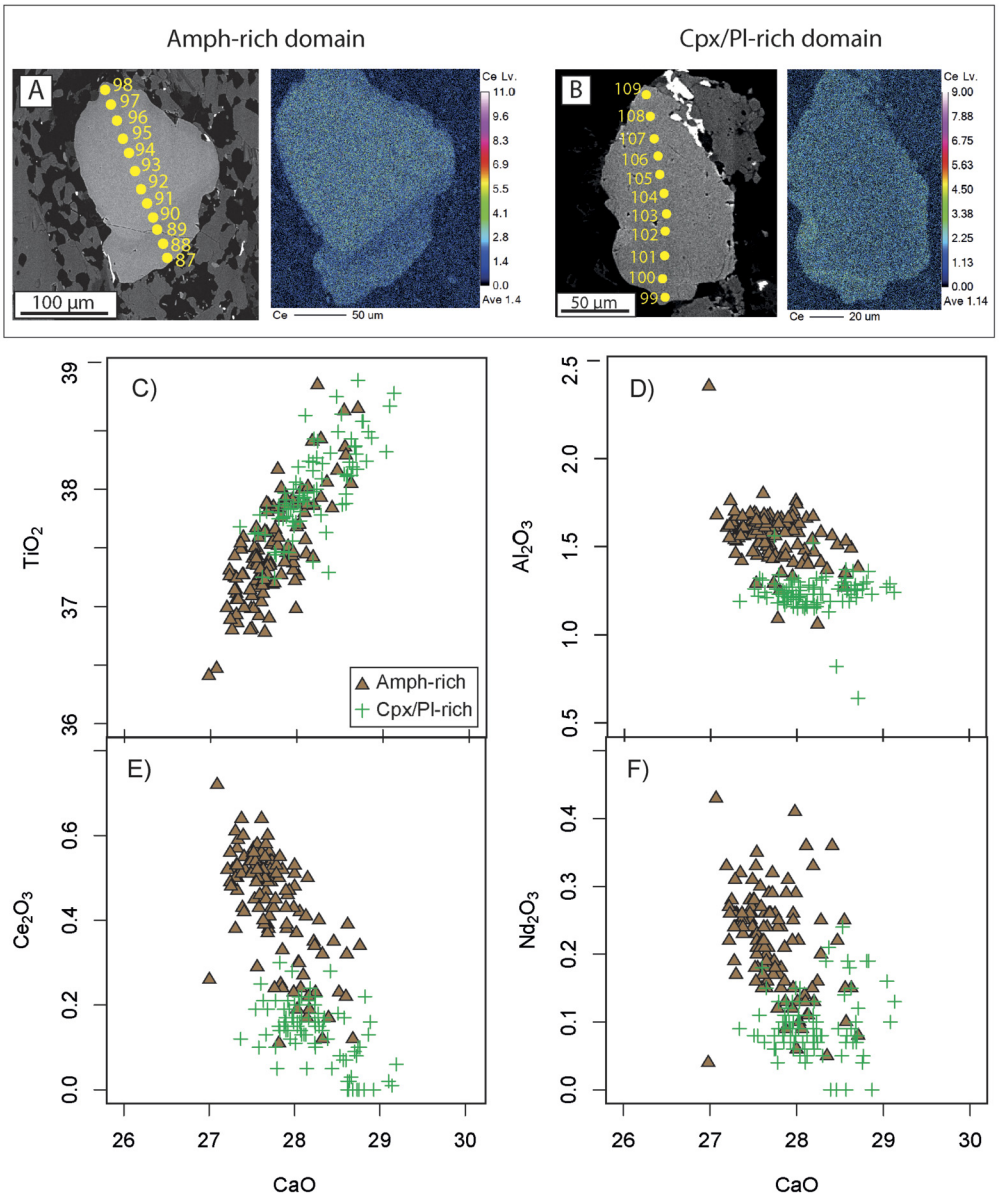


**Fig. 5.** Titanite BSE-SEM images, X-ray maps and EPMA chemical diagrams for the studied microdomains. A, B) BSE-SEM and X-ray map for Ce from Amph-rich and Cpx/Pl-rich domains, respectively. Yellow points and number refer to the EPMA data profile performed for each titanite and reported in Table S2. C, D, E, F) Titanite for the two different compositional domains showing CaO versus: A) $TiO_2$; B) $Al_2O_3$; C) $Ce_2O_3$; D) $Nd_2O_3$.

± 0.1 wt.%), $Ce_2O_3$ (0.11 ± 0.07 → 0.14 ± 0.09 wt.%) and $Nd_2O_3$ (0.08 ± 0.05 → 0.11 ± 0.06 wt.%; Fig. 5C-F). As highlighted by X-ray maps, $Ce_2O_3$ and $Nd_2O_3$ show opposite core to rim zoning with respect to titanite from Amph-rich domains (Figs. 5; S4).

By comparing the titanite quantitative chemical analyses and X-ray maps from the two different compositional domains, several chemical differences, larger that the analytical errors, are apparent (Table S2; Fig. 5C-F). Titanite from Amph-rich domains is generally poorer in CaO (27.71 ± 0.35 wt.%) and $TiO_2$ (37.47 ± 0.44 wt.%) content with respect to titanite from Cpx/Pl-rich domains (CaO 28.20 ± 0.40 wt.%, $TiO_2$ 38 ± 0.37 wt.%; Table S2; Fig. 5). Conversely, titanite from Cpx/Pl-rich domains has lower $Al_2O_3$ (1.24 ± 0.11 wt.%), $Ce_2O_3$ (0.13 ± 0.07 wt.%) and $Nd_2O_3$ (0.10 ± 0.05 wt.%) with respect to titanite from Amph-rich domains ($Al_2O_3$ 1.56 ± 0.15 wt.%, $Ce_2O_3$ 0.44 ± 0.13 wt.%, and $Nd_2O_3$ 0.22 ± 0.07 wt.%; Table S2; Fig. 5).

### 4.4. U–Pb LASS-ICP-MS in-situ chronology

#### 4.4.1. Amphibole-rich domains

The results of 108 *in-situ* analyses on 14 titanite grains are summarized in Table S1 and Fig. 6. U–Pb data plotted on the Tera-Wasserburg diagram define a large U–Pb field suggesting ternary mixing between a common Pb component and multiple radiogenic Pb components (e.g., Stearns et al., 2015).

A robust correlation between titanite microstructure, measured as average dislocation density, and U–Pb data is lacking (Fig. 6A). Nevertheless, a subset of U–Pb data points could be defined by spot analyses of grain rims with significant lattice distortions, sub-grains and newly nucleated grains (12 spots from three T2 grains, 31 spots from eight T3 grains; Fig. 6A). Part of these textures display local high dislocation density (>0.002 $\mu m^{-1}$, 14 spots; Fig. 6A; Table S1).

A clearer subset of U–Pb data points (n = 29) is distinct in terms of geochemical signature (Fig. 6B-E). It is defined by high $^{207}Pb/^{206}Pb$ ratios (>0.2), which are inversely correlated with re-

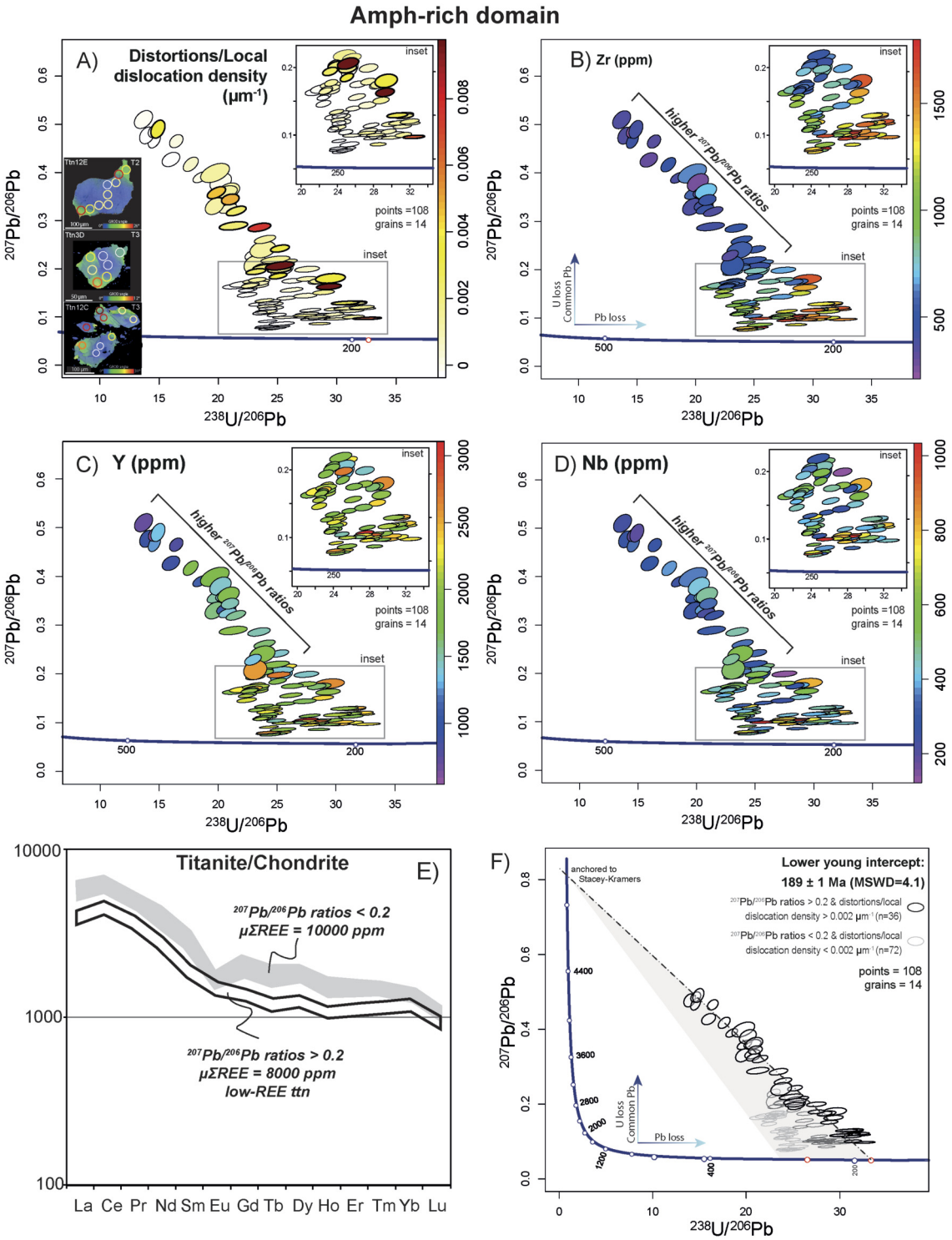


**Fig. 6.** Titanite U–Pb data yielded for Amph-rich domains and representative correlations with: A) lattice distortions/local dislocation density ($\mu m^{-1}$) and trace-elements concentrations for: B) Zr (ppm), C) Y (ppm), D) Nb (ppm). In A) the box top right report U–Pb data and textural/microstructural correlation highlighting high distortions/local dislocation density values. E) Chondrite-normalized REE patterns of titanite in Amph-rich domains according to McDonough and Sun (1995); the $\mu\sum$REE and $\sum$REE refer to the average and sum of REE, respectively. F) Tera-Wasserburg concordia plots summarizing titanite U–Pb data. The lower intercept age is obtained from U–Pb data with petrochronological and microstructural correlations (low-REE ttn; $^{207}Pb/^{206}Pb$ ratios > 0.2 & distortions/local dislocation density > 0.002 $\mu m^{-1}$) highlighted with thicker black circles.

spect to REE, Zr, Y, Nb (Fig. 6B-E) and U (being mostly lower than 113ppm; Table S1). Moreover, the chondrite normalized REE patterns of this subset show modestly lower concentrations as well as a lack of an apparent Eu negative anomaly (Fig. 6E). This population of petrochronological data (hereafter, low-REE ttn) correlates with spots collected from grain rims, subgrains and two newly nucleated grains, mostly characterized by an average local dislocation density greater than 0.002 $\mu m^{-1}$ (7 spots; Fig. 6A-D; Table S1). By combining the U–Pb data points from the low-REE ttn and the points with local high dislocation density >0.002 $\mu m^{-1}$, an isochron with a lower intercept age of 189 ± 1 Ma can be defined (MSWD = 4.1; n = 36; Fig. 6F).

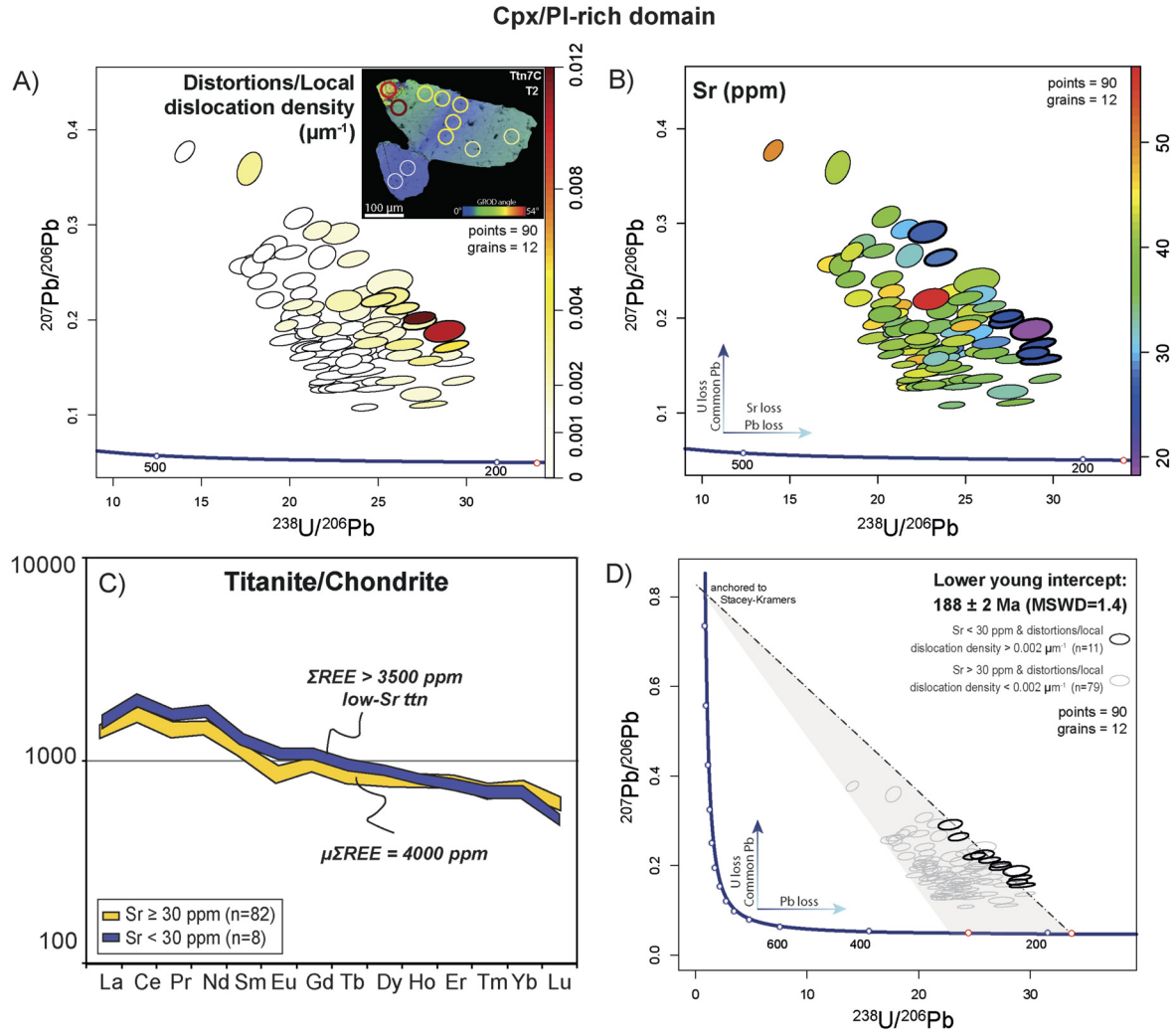


**Fig. 7.** Titanite U–Pb data yielded for Cpx/Pl-rich domains and representative correlations with: A) lattice distortions/local dislocation density ($\mu m^{-1}$) and B) trace-elements concentrations, i.e., Sr (ppm). In A) the box top right report U–Pb data and textural/microstructural correlation showing high distortions/local dislocation density values. C) Chondrite-normalized REE patterns of titanite in Cpx/Pl-rich domains according to McDonough and Sun (1995) the $\mu\sum$REE and $\sum$REE refer to the average and sum of REE, respectively. D) Tera-Wasserburg concordia plots summarizing titanite U–Pb data. The lower intercept age is obtained from U–Pb data with petrochronological and microstructural correlations (low-Sr ttn; Sr <30 ppm & distortions/local dislocation density > 0.002 $\mu m^{-1}$) highlighted with thicker black circles.

*4.4.2. Clinopyroxene/plagioclase-rich domains*

A total of 90 petrochronological analyses were performed on 12 grains and are summarized in Table S1 and Fig. 7. As for Amph-rich domains, the U–Pb data are dispersed on the Tera-Wasserburg diagram defining a large U–Pb field suggesting ternary mixing between a common Pb component and multiple radiogenic Pb components (e.g., Stearns et al., 2015).

By considering the average dislocation density calculated for each U–Pb analytical spot no clear correlations are apparent (Fig. 7A). However, data collected from titanites with significant lattice distortions, i.e., distorted grain rims and subgrains, define a subset of 26 points (25 spots from five T2 grains, 1 spot from one T3 grain; Fig. 7A). Although titanite domains showing an average dislocation density higher than 0.002 $\mu m^{-1}$ mostly clustered in a narrower U–Pb space, they do not define a single isochron (7 spots; Fig. 7A; Table S1).

In comparison with Amph-rich domains, the U–Pb data of titanite from the Cpx/Pl-rich domains show a weaker correlation with geochemistry (Fig. 7B, C). Among the analyzed trace elements, only Sr shows an apparent correlation with the U–Pb isotopic data. Analyses with a Sr value lower than 30 ppm broadly define a subset on the U–Pb space (8 spots from five T2 grains). This population (hereafter low-Sr ttn) is further characterized by slightly higher L- and M-REE concentrations with respect to the other data points (Fig. 7B, C). The low-Sr ttn include some spots (n = 4) performed on titanite rims or subgrains with high local dislocation density (>0.002 $\mu m^{-1}$; Fig. 7A, B; Table S1). The U–Pb data from low-Sr ttn and high local dislocation density rims define an alignment with a lower intercept age of 188 ± 2 Ma (MSWD = 1.4; n = 11; Fig. 7D).

## 5. Discussions

### 5.1. Origin and petrologic evolution of titanite

In order to discriminate the possible origin of the studied titanite, we plotted Al/Fe versus $\sum$LREE (Fig. S5A) and Fe content versus Zr/Y (Fig. S5B) according to Scibiorski et al. (2019) and Scibiorski and Cawood (2022). Although titanite grains from the two compositional domains define distinct clusters on the Al/Fe versus $\sum$LREE diagram, they fall in the field of metamorphic titanite (Al/Fe = 1-10; $\sum$LREE = 1000-10000; Fig. S5A). The Fe versus Zr/Y diagram (Fig. S5B) suggests that titanite from the Amph-rich and Cpx/Pl-rich domains is compatible with mafic (i.e., amphibolites) and calc-silicate protoliths (Fe = 1000-10000; Zr/Y = 1 for Cpx/Pl-rich layer, Zr/Y = 0.1-1 for Amph-rich domains), as pre-

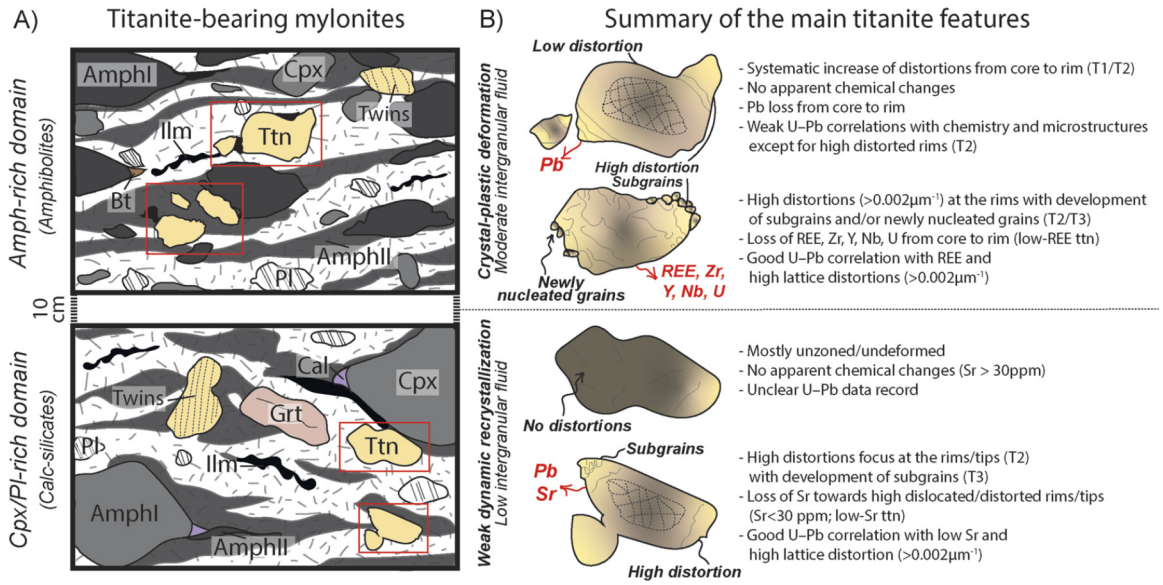


**Fig. 8.** Summary of textural/microstructural features of titanite and host rocks. A) Schematic representation of rock microdomain textures and titanite described in the text. The cartoons were drawn following the representative compositional rock domains (Amph-rich and Cpx/Pl-rich) viewed at the microscale (mm-cm), such that the grain size and mineralogical relationships are accurately represented. B) Summary of the main petrochronological, textural and microstructural titanite features from the microdomains following the main distinctions criteria and results as described through the text. Dark brown color and dashed black lines refer to no and low lattice distortion/dislocations domains and chemical variations, whereas the light brown color and black lines indicate the high lattice distortions/dislocations portions as well as the chemical changes. Titanite developed different features as function of microstructural features and locally showing chemical changes with main mineral phases.

viously demonstrated on the basis geochemistry and petrography (Corvò et al., 2022).

In general, the observed decoupling of BSE, chemical zoning and lattice distortions (e.g., Figs. 4ii, 6A) suggests that a pre-kinematic zoning persisted throughout deformation and/or fluid grain interaction and was likely related to the titanite growth within different protoliths (Fig. 8A). The titanite-forming reactions occurred coevally with the mineral assemblages, which is ascribable to the high-temperature regional metamorphism recorded at the mid-low crustal levels (from 650 to 820 °C, 0.7-0.8 GPa; Corvò et al., 2022 and references therein). In the Amph-rich domains, microstructures suggest the formation of titanite by the reactions: Zo (or Ep) + Chl + Qz = Ca-Amph + An + $H_2O$ (Spear, 1993) or Cpx + Ilm + Qz + $H_2O$ = Ca-Amph + Ttn (Frost et al., 2000). The Cpx/Pl-rich domains, with rare calcite but without quartz at the peak metamorphic conditions, likely developed as consequence of the following reaction: Qz + Cal + Tr + Rt = Cpx + $CO_2$ + $H_2O$ + Ttn (e.g., Walters et al., 2022). In both compositional microdomains, the presence of a Ti-bearing phase (e.g., ilmenite or rutile) among the reactants may have promoted the formation of titanite. Moreover, the developed mineral assemblages within both compositional domains influenced the chemistry of titanite. The lower $TiO_2$ content of titanite from the Amph-rich domains with respect to those from the Cpx/Pl-rich ones is compatible with an abundant crystallization of pargasite, with $TiO_2$ up to 2.5 wt.% (Corvò et al., 2022), coevally with titanite (Figs. 5C; 8A). Analogously, the lower content of $Al_2O_3$ and LREE of titanite from Cpx/Pl-rich domains with respect to titanite from Amph-rich ones (Fig. 5D-F) suggests the formation of titanite in a plagioclase dominated environment where $Al_2O_3$ and LREE were fractionated within the feldspar (Corvò et al., 2022).

In both compositional domains, titanite grains were affected by limited trace-element variations during deformation (Figs. 6B-E; 7B-C). The most appreciable geochemical variations are observed in subgrains and newly nucleated grains from Amph-rich domains (T3, Figs. 3F, G; 8B). These domains show REE patterns almost parallel with respect to the REE patterns of other titanite grains/domains but at lower concentrations and without apparent Eu negative anomaly (Fig. 6E). Moreover, they are further characterized by lower concentration of Zr, Y, Nb and U (Fig. 6B-D). All these geochemical features associated with microstructures can be related to the element mobility enhanced by deformation (Figs. 6A; 8A, B). Indeed, it has been demonstrated that deformation can promote intragrain physical and/or chemical changes of highly resistant accessory minerals such as zircon, chromite, and rutile (Piazolo et al., 2012, 2016; Satsukawa et al., 2015; Smye et al., 2018) as well as silicate porphyroclasts (e.g., Lund et al., 2006; Corvò et al., 2020). The chemical variations associated with subgrains and/or newly nucleated grains imply fluid-assisted chemical exchanges between titanite and other syn-kinematic minerals (McGregor et al., 2021; Erickson et al., 2015). In the Amph-rich domain, the lower concentrations of REE and other trace-elements (low-REE ttn population) reflect the abundant crystallization of syn-kinematic amphibole (AmphII), epidote and ilmenite at amphibolite-facies conditions (Fig. S1). As documented by Corvò et al. (2022), the mylonitization induced significant variations in the mineral composition, although the mineral assemblage remained the same. The amphibole changes from pargasite (AmphI) to a more edenite/hornblende (AmphII) composition. In the same way, the recrystallized plagioclase is less anorthitic with respect to the neighboring porphyroclasts (Corvò et al., 2022).

In contrast, titanite from the Cpx/Pl-rich domains generally does not show clear chemical variations correlated with BSE textures and/or microstructures (Fig. 7). The only exception is represented by the low-Sr ttn population, partially corresponding with domains showing high lattice distortion and high local dislocation density. This correlation could reflect a zoning due to chemical exchange between titanite and other Sr-rich mineral phases formed during deformation (e.g., plagioclase, epidote, and calcite; Fig. 8A, B). The local occurrence of calcite within clinopyroxene tails suggests the formation of syn-kinematic calcite, likely controlling the Sr depletion of the titanite external domains (Fig. S1C, D).

The lack of a pronounced negative Eu anomaly within the REE patterns of the syn-kinematic titanite populations in both compositional domains is the result of the ability of the titanite to fractionate more efficiently L- and M-REE than the recrystallizing plagioclase. Finally, the LREE depletion in the Amph domains ver-

sus the Sr depletion in the Cpx/Pl domains is clear evidence of the differences in local chemical environments and reactivity of phases likely in presence of a given fluid composition.

### 5.2. Interpretation of titanite microstructures

To date, few studies on titanite microstructural features are available. Granular texture, neoblastic microstructures and deformation twins have been described mainly as the result of meteorite impact events (e.g., Borg, 1970; Borg and Heard, 1972; Papapavlou et al., 2018; Timms et al., 2019; McGregor et al., 2021). Other studies (i.e., Gordon et al., 2021; Cavosie et al., 2022) describe aggregates of neoblastic titanite experienced multiple phases of growth, crystal-plastic deformation, and fluid-mediated recrystallization during multistage high-temperature metamorphism. Finally, Moser et al. (2022) show that lattice bending and dissolution–reprecipitation are coupled processes both resulting in a reset of dates and trace-element signatures, but the relative contribution of each process remains difficult to resolve.

We interpret that titanites from our study are mostly pre-kinematic, based on their shape, large size and relation to the general microstructure and chemistry. Our quantitative orientation analysis shows that titanite from both compositional domains commonly exhibits sets of twins with a disorientation relationship from the host grain of 74°/<-10-2> (Figs. 3Ciii, Fiii, 4Cii, Giii), while only few grains locally show slightly kinked or/and tapered twins (Fig. 4Eii). We do not observe a compositional and textural control on the development of these sets of twins. Most of the weakly-deformed grains present twins crosscutting the whole crystal (Figs. 3Ciii, Fiii; 4Cii, Giii), while a minor number of straight twins affects the bent domains (Fig. 4Eii). Papapavlou et al. (2018) summarized the origin of twins as generated by: (i) lattice defects during growth of a crystal (growth twins), (ii) phase transformations (transformation twins), (iii) application of shear stresses on a crystal (deformation twins). Only few authors describe deformation twins in titanite as a result of typical endogenic tectonometamorphic conditions (e.g., Spencer et al., 2013; Bonamici et al., 2015).

We interpret the straight twins to be part of the pre-kinematic growth of titanite (Figs. 3Ciii, Fiii, 4Cii, Giii), while only the kinked and tapered twins are related to crystal-plastic deformation (Fig. 4Eii). Interestingly, the lack of correlation between twin and elemental variations within titanite grains (Figs. 6, 7) suggests that twins, at the conditions experience by the studied rocks (650-820 °C, 0.7-0.8 GPa; Corvò et al., 2022) could either enhance or inhibit diffusion (e.g., Bonamici et al., 2015).

Detailed orientation analyses shows that there is systematic lattice bending localized in the rims/tips of titanite grains, particularly in the Amph-rich domains (Fig. 8B). Titanites investigated here reveal a mix of weakly, highly distorted domains and newly nucleated grains (Fig. 6A, 7A). Grains from the Amph-rich domains occur mostly as elongated/sigmoidal shapes characterized by clear evidence of lattice bending, revealed by significant internal distortions (T3; up to ∼30°; Fig. 3). Misorientations are either progressively or abruptly increasing from core to rim and are significantly developed along systematic confined disorientation axes and slip planes (T2/T3; Figs. 2, 3; Piazolo et al., 2012; Moser et al., 2022). A few grains of T3 show more complex features, including: i) weak internal distortion (reflected by a less pronounced BSE core-rim zoning, e.g., Fig. 2I); ii) inhomogeneous, patchy distributed, internal distortion forming aggregates of grains, iii) development of distinct grains with low distortion and different orientations (Fig. 3F, G). These latter individual grains are interpreted as newly nucleated grains which 1) grew spontaneously adjacent to highly deformed larger grains and 2) show low internal dislocation density (also termed heterogeneous nucleation e.g., Cantor, 2003). This spontaneous growth may be enhanced by chemical driving forces associated with fluid-mediated replacement reactions, resulting in grains of different orientation and distinct chemistry (e.g., Putnis and Austrheim, 2010; Piazolo et al., 2012; Satsukawa et al., 2015; Spruzeniece et al., 2017; Gordon et al., 2021).

Although there are interesting similarities in the textural and microstructural features of titanite in the different compositional domains (see T2 and T3 groups, Figs. 3, 4, exception for 3F, G), statistically, titanite from the Amph-rich domains recorded better the deformation with respect those from the Cpx-Pl-rich domains (Amph-rich: 19/23 deformed grains; Cpx/Pl-rich: 10/30 deformed grains). Overall, microstructural patterns indicate that titanite from Amph-rich domains mainly deformed by crystal-plastic mechanisms where high lattice distortions focused along the grain boundaries resulting in highly chemically re-equilibrated strained rims/tips (e.g., Piazolo et al., 2012, 2016; Gordon et al., 2021; Moser et al., 2022). Grain bending was accompanied by minor recrystallization, resulting in newly nucleated grains mediated by deformation and intergranular fluid. On the other hand, mostly unzoned grains from Cpx/Pl-rich domains, some characterized by a small variation of crystallographic orientation increasing towards the rims (T1/T2), are evidence of weak crystal-plastic deformation localized in narrow and discontinuous rims/tips. Lattice bending in these titanite grains does not result in a significant change in chemistry (Fig. 8A, B).

### 5.3. U–Pb age interpretation and correlation with microstructure and chemistry

In both Amph- and Cpx/Pl-rich domains, U–Pb dates are correlated with different titanite populations, distinguished by chemistry and/or microstructural signatures (Fig. 8A, B). In particular, U–Pb data provides Jurassic lower intercept ages (∼189 Ma, Fig. 9A) for titanite domains showing distinct chemical signatures mostly corresponding with tips/rims/subgrains with high local dislocation density (>0.002 $\mu m^{-1}$) and/or newly nucleated grains (Figs. 6, 7). The correlation among chemistry, microstructures and U–Pb data is likely due to the crystal-plastic deformation (e.g., Piazolo et al., 2012, 2016) and indicates the reactivity of titanite during deformation in presence of fluids (e.g., Gordon et al., 2021). The chemical signatures acquired by titanite during deformation (e.g., low-REE ttn within Amph-rich domains, low-Sr ttn within Cpx/Pl-rich domains) imply the involvement of other accessory or main mineral phases containing Pb, U (e.g., plagioclase or other U-bearing phases, e.g., Kirkland et al., 2018) and other trace elements (e.g., syn-kinematic amphibole, epidote, biotite and ilmenite). Deformation enhanced the reactivity of titanite, promoting chemical exchanges between titanite and the surrounding mineral phases (Fig. 8A, B). The fact that such deformation related enhancement is better recorded within titanite from Amph-rich domains, suggests that the reactivity of the investigated geochronometer is heterogeneous at the thin-section scale and is influenced by the chemical composition of the hosting rock microdomain (Figs. 7, 8). We thus interpret the lower Jurassic intercept ages (∼189 Ma) from the chemically modified and/or recrystallized/deformed titanite as a constraint for the amphibolite-facies deformation activity of the shear zone (Fig. 9A).

Despite the good correlation observed for a few titanite domains, the remaining dataset do not allow to define clear relationships among chemistry, isotopes, and microstructure. Ambiguous and unsystematic correlations between U–Pb data, titanite orientation changes and smeared out trace-element composition have been recently documented and associated to multiple processes, including diffusion, deformation, replacement-reactions, and fluid-mineral interaction (i.e., Garber et al., 2017; Gordon et al., 2021; Moser et al., 2022). It is argued, indeed, that these processes pro-

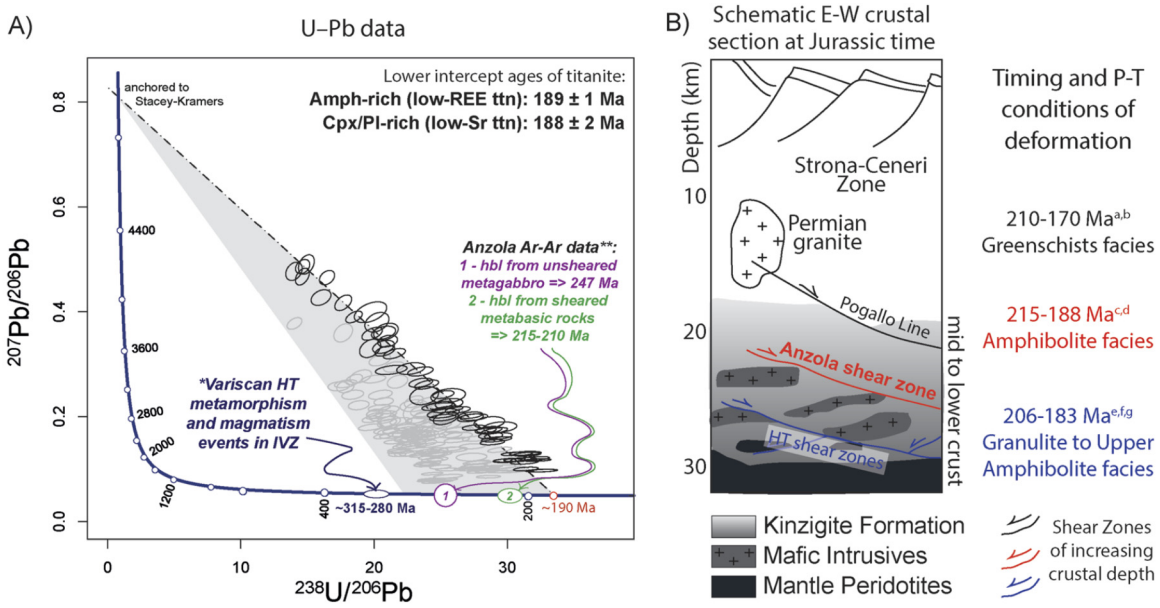


**Fig. 9.** Summary of U–Pb geochronological analysis of titanite on the studied rock compositional domains and schematic Ivrea-Verbano crustal section. A) Complete U–Pb dataset of this work with particular highlights on the lower intercept ages (black circles and black dashed line). Other references data are reported: * = geochronological literature data from Köppel (1974) and Klötzli et al. (2014); ** = geochronological literature data from Brodie et al. (1989). B) Schematic crustal section of the Jurassic passive continental margin in the Southern Alps (modified after Langone et al., 2018), showing the Anzola shear zone and other extensional faults at different crustal levels. Available timing and P–T conditions of deformation are reported in a: Ar-Ar on white mica (Mulch et al., 2002); b: K-Ar on micas (Wolff et al., 2012); c: U–Pb on titanite (this work); d: Ar-Ar on hornblende (Brodie et al., 1989); e: Ar-Ar on hornblende (Boriani and Villa, 1997); f: U–Pb on zircon (Langone et al., 2018); g: U–Pb on zircon (Corvò et al., 2020).

vide a mixture between original and newly equilibrated fluid composition in both its isotopic and chemical signature (Varga et al., 2020).

Except for the two recognized petrochronological populations for both compositional domains, the remaining dataset does not allow a clear interpretation (Fig. 9A). The lack of isotopic alignment correlated with chemistry and/or microstructures could be interpreted as the result of: i) a later isotopic "smearing" out of the initial metamorphic growth age due to coupled dissolution-precipitation process (e.g., Varga et al., 2020); ii) volume diffusion process with partial U–Pb resetting, occurring between the metamorphic crystallization and deformation (e.g., Moser et al., 2022), iii) a combination any or all of the above. In absence of correlation with textural position and chemistry, the U–Pb dataset cannot be discussed without the geological framework and, therefore, an attempt to interpret their geological significance is provided in the section 5.5.

### 5.4. Fluid-mineral interaction

The complexity in titanite U–Pb dating derives from the challenge to correlate U and Pb mobility with either fluid-mediated replacive processes or fast diffusion along arrays of lattice defects (Garber et al., 2017; Gordon et al., 2021; Moser et al., 2022). Our study focused on titanite from layers with mineral assemblages characterized by a different composition and reactivity (Corvò et al., 2022). As discussed in previous sections, titanites from the Amph-rich domains display evidence of intergranular fluids that locally promoted replacement reaction processes (i.e., low-REE ttn; Figs. 3F, G, 7, 8). The presence of fluids during deformation is further documented by the widespread occurrence of syn-kinematic hydrous mineral phases such as amphibole (AmphII) and rarely biotite (Fig. 8). Conversely, the mineral assemblage of the Cpx/Pl-rich domains does not show evidence of abundant reaction with fluids during deformation (Figs. 2, S1). This is documented by the extensive dynamic recrystallization of clinopyroxene and plagioclase with minor occurrence of syn-kinematic calcite and hydrous mineral phases (i.e., amphibole; Figs. 2, S1). The limited intragrain chemical variation of titanite (e.g., Sr depletion of the titanite rims/tips) from this domain is a further consequence of the low fluid activity/reactivity during deformation.

The observed different reactivity cannot be due to different P-T conditions as the two domains are interlayered at the mm- to cm-scale. Instead, our data are consistent with different chemical reactivity, more pronounced for Amph-rich domains, mainly influenced by the bulk rock composition of the host rocks (mafic rocks vs. calc-silicates) combined with locally derived fluids. This process promotes continuous dissolution, precipitation and lattice diffusion through subgrains boundaries during recrystallization and crystal plastic deformation (Fig. 8; Putnis and Austrheim, 2010). In contrast, a syn-tectonic pervasive fluid flux, i.e., high fluid rock ratios, would have promoted, at the known P-T conditions, the partial replacement of former mineral assemblages with new ones dominated by hydrous mineral phases.

Our data show that titanite in both compositional domains have U–Pb systematics reset but the indicators and proxies used to recognize these resets of titanite dates are different. In the Amph-rich domains, the simultaneous activity of crystal-plastic deformation causing rearrangements at the lattice scale, results in a clear correlation of chemical, microstructural and isotopic signatures. This correlation is more subtle in the titanite from the Cpx/Pl-rich domains, where syn-tectonic, spatially restricted replacement reactions result in minor chemical changes and developing of microstructural features as well as minor correlation with isotopic signature. We thus suggest that, to date deformation in high strain zones deforming at low fluid-rock ratios under amphibolite-facies conditions, hydrous protoliths are the most suitable candidates.

### 5.5. Regional implications of the Ivrea-Verbano Zone during the Triassic-Jurassic rifting event

The cumulative lower intercept age at 189 ± 2 Ma from titanite petrochronology marks the end of the upper amphibolite-facies deformation that likely encompasses several Myr (Triassic-Jurassic

times) as documented by the $^{40}Ar/^{39}Ar$ ages of ~215-210 obtained by Brodie et al. (1989) on syn-kinematic hornblende from the Anzola shear zone (Fig. 9A).

Ductile deformation has been constrained at the Triassic-Jurassic boundary within upper and lower crustal levels of the Ivrea-Verbano Zone (Fig. 9B), respectively: the greenschist-facies Pogallo Line (210-170 Ma; Zingg, 1990; Mulch et al., 2002; Wolff et al., 2012) and granulite/amphibolite-facies shear zones exposed in Val Cannobina (206-183 Ma; Boriani and Villa, 1997; Langone et al., 2018). The activity of the Anzola shear zone is, within error, simultaneously with other structures at different crustal levels. This is in agreement with the tectonic thinning regime predicted for the Ivrea-Verbano crustal section during the late Triassic-early Jurassic rifting event, where deformation started to localize along a number of ductile shear zones which efficiently thinned the middle to lower crust (Manatschal et al., 2007; Beltrando et al., 2015; Petri et al., 2019).

Even though the dataset that cannot be related to this latter event could be interpreted as a possible older lower intercept age at the early Permian, its interpretation remains enigmatic (Fig. 9A). We note that this dataset could be entirely geologically meaningless due to a partial U–Pb resetting associate with incomplete diffusion and/or recrystallization processes (Varga et al., 2020; Moser et al., 2022). Notably, the time interval preceding the Triassic-Jurassic deformation, the IVZ was affected by magmatism and metasomatism at different crustal levels (e.g., Locmelis et al., 2016; Langone et al., 2017) as well as by extensive HT regional metamorphism protracted for several Myr (e.g., Vavra et al., 1999; Ewing et al., 2013; Kunz et al., 2018). All these processes may have affected the U–Pb data of the titanite after its initial growth. Moreover, it must be taken into account that the emplacement age of the neighboring Anzola gabbro has not been well constrained yet. A minimum $^{40}Ar/^{39}Ar$ age of ~247 Ma on hornblende was obtained by Brodie et al. (1989) and interpreted as related to the cooling stage. It is worth noting that the possible older isochron delimiting the dataset is roughly co-linear with the reported $^{40}Ar/^{39}Ar$ cooling age of Brodie et al. (1989) (point 1 on Fig. 9A) and is probably linked to the end of the gabbro-induced thermal perturbation. Thus, to access a possible geological meaning of the pre-shear zone activity titanite dataset, further geochronological investigations on different geochronometers are still needed.

## 6. Conclusions

We performed a petrochronological and microstructural study on titanite grains from the compositionally variable mylonites of the Anzola shear zone (Southern Alps, Italy).

This study reveals that:

– although mylonites experienced the same P-T conditions, titanite shows different textural, microstructural and compositional features at the mm- to cm-scale as a function of the hosting microdomain composition (calc-silicate vs. amphibolites);

– titanite from Amph-rich domains displays a higher degree of intracrystalline deformation dominated by crystal-plasticity, and more apparent and systematic chemical variations which correlate with the observed deformation features. Conversely, in Cpx/Pl-rich domains titanite shows minor evidence of deformation; here crystal plastic deformation features are mainly restricted to lattice bending localized in narrow areas associated with titanite rims/tips, and weaker chemical variation signatures with no clear correlation with the narrow deformation areas;

– the robust coupling of U–Pb petrochronology within Amph-rich domains with deformation microstructures allows to constrain the ductile deformation under amphibolite-facies at Jurassic time (~189 Ma).

Despite the complexity and uncertainties related to titanite growth and recrystallization, U–Pb petrochronology may be used to date the timing of high-temperature crystal-plastic deformation. Overall, the success of this approach is dependent on the monitoring of several concurring factors: microdomain composition and reactivity, fluid availability, intensity of intracrystalline deformation.

Finally, we suggest that in lithological heterogeneous mylonites containing titanite deformed without presence of a pervasive and externally derived fluid, the best candidates for dating deformation are host rocks with relatively abundant hydrous phases. These ones can release local fluids interacting with the other pre-existing phases, promoting simultaneous crystal-plastic deformation and the formation of new grains. This results in an overall increase of the titanite reactivity, which allows the titanite chemically adjust syn-tectonically.

## CRediT authorship contribution statement

**Stefania Corvò:** Writing – original draft, Visualization, Validation, Methodology, Investigation, Formal analysis, Conceptualization. **Matteo Maino:** Writing – review & editing, Validation, Supervision, Investigation, Conceptualization. **Sandra Piazolo:** Writing – review & editing, Validation, Methodology, Data curation. **Andrew R.C. Kylander-Clark:** Writing – review & editing, Validation, Methodology, Data curation. **Andrea Orlando:** Writing – review & editing, Validation, Methodology, Data curation. **Silvio Seno:** Supervision, Funding acquisition. **Antonio Langone:** Writing – review & editing, Validation, Supervision, Methodology, Investigation, Funding acquisition, Data curation, Conceptualization.

## Declaration of competing interest

The authors declare that they have no known competing financial interests or personal relationships that could have appeared to influence the work reported in this paper.

## Acknowledgements

We wish to thank SWISSTOPO, SUPSI (Swiss; project n°.12RAFGOSO and n°.12RA1CARTOTIGR) and IGG-C.N.R., for their financial, instruments and laboratories support (PRIN2017 “Micro to Macro—how to unravel the nature of the large magmatic events; 20178LPCPWLangoneAntonio”). Part of the analyses were performed by Stefania Corvò at School of Earth and Environment, University of Leeds (Leeds, UK) during a short mobility period of PhD scholarship provided by Università di Pavia (Bando di Mobilità Internazionale 2019 - 8ª edizione). We very appreciated the helpful and constructive reviews of Craig Storey and two anonymous reviewers, as well as Alex Webb for his editorial handling.

## Appendix A. Supplementary material

Supplementary material related to this article can be found online at https://doi.org/10.1016/j.epsl.2023.118349.

## References

Beltrando, M., Stockli, D.F., Decarlis, A., Manatschal, G., 2015. A crustal-scale view at rift localization along the fossil Adriatic margin of the Alpine Tethys preserved in NW Italy. Tectonics 34, 1927–1951.

Bestmann, M., Piazolo, S., Spiers, C.J., Prior, D.J., 2005. Microstructural evolution during initial stages of static recovery and recrystallization: new insights from in-situ heating experiments combined with electron backscatter diffraction analysis. J. Struct. Geol. 27, 447–457.

Bonamici, C.E., Blum, T.B., 2020. Reconsidering initial Pb in titanite in the context of in situ dating. Am. Mineral. 105 (11), 1672–1685.

Bonamici, C.E., Fanning, C.M., Kozdon, R., Fournelle, J.H., Valley, J.W., 2015. Combined oxygen-isotope and U-Pb zoning studies of titanite: new criteria for age preservation. Chem. Geol. 398, 70–84.
Borg, I.Y., 1970. Mechanical <110> twinning in shocked sphene. Am. Mineral. 55, 1876–1888.
Borg, I.Y., Heard, H.C., 1972. Mechanical twinning in sphene at 8 Kbar, 25° to 500 °C. Geol. Soc. Am. Mem. 132, 585–592.
Boriani, A., Villa, I.M., 1997. Geochronology of regional metamorphism in the Ivrea-Verbano Zone and Serie dei Laghi, Italian Alps. Schweiz. Miner. Petrogr. 77, 381–402.
Brodie, K.H., Rutter, E.H., Rex, D., 1989. On the age of deep crustal extensional faulting in the Ivrea zone, Northern Italy. Geol. Soc. (Lond.) Spec. Publ. 45, 203–210.
Cantor, B., 2003. Heterogeneous nucleation and adsorption. Philos. Trans. R. Soc. Lond. A, Math. Phys. Eng. Sci. 361 (1804), 409–417.
Cavosie, A.J., Spencer, C., Evans, N., Rankenburg, K., Thomas, R.J., Macey, P.H., 2022. Granular titanite from the roter kamm crater in Namibia: product of regional metamorphism, not meteorite impact. Geosci. Front., 101350.
Cherniak, D.J., 1993. Lead diffusion in titanite and preliminary results on the effects of radiation damage on Pb transport. Chem. Geol. 110, 177e194.
Cherniak, D.J., 2010. Diffusion in accessory minerals: zircon, titanite, apatite, monazite and xenotime. Rev. Mineral. Geochem. 72 (1), 827–869.
Corvò, S., Langone, A., Padrón-Navarta, J.A., Tommasi, A., Zanetti, A., 2020. Porphyroclasts: source and sink of major and Trace Elements during deformation induced metasomatism (Finero, Ivrea-Verbano Zone, Italy). Geosciences 10, 196.
Corvò, S., Maino, M., Piazolo, S., Seno, S., Langone, A., 2022. Role of inherited compositional and structural heterogeneity in shear zone development at mid-low levels of the continental crust (the ASZ; Ivrea-Verbano Zone, Southern Alps). Lithos, 106745.
Denyszyn, S.W., Fiorentini, M.L., Maas, R., Dering, G., 2018. A bigger tent for CAMP. Geology 46 (9), 823–826.
Erickson, T.M., Pearce, M.A., Taylor, R.J.M., Timms, N.E., Clark, C., Reddy, S.M., Buick, I.S., 2015. Deformed monazite yields high-temperature tectonic ages. Geology 43 (5), 383–386.
Ewing, T.A., Hermann, J., Rubatto, D., 2013. The robustness of the Zr-in-rutile and Ti-in-zircon thermometers during high-temperature metamorphism (Ivrea-Verbano Zone, Northern Italy). Contrib. Mineral. Petrol. 165, 757–779.
Frost, B.R., Chamberlain, K.R., Schumacher, J.C., 2000. Sphene (titanite): phase relations and role as a geochronometer. Chem. Geol. 172 (1–2), 131–148.
Garber, J.M., Hacker, B.R., Kylander-Clark, A.R.C., Stearns, M., Seward, G., 2017. Controls on trace element uptake in metamorphic titanite: implications for petrochronology. J. Petrol. 58 (6), 1031–1057.
Gordon, S.M., Kirkland, C.L., Reddy, S.M., Blatchford, H.J., Whitney, D.L., Teyssier, C., McDonald, B.J., 2021. Deformation-enhanced recrystallization of titanite drives decoupling between U–Pb and trace elements. Earth Planet. Sci. Lett. 560, 116810.
Hayden, L.A., Watson, E.B., Wark, D.A., 2008. A thermobarometer for sphene (titanite). Contrib. Mineral. Petrol. 155, 529e540.
Holder, R.M., Hacker, B.R., 2019. Fluid-driven resetting of titanite following ultrahigh-temperature metamorphism in southern Madagascar. Chem. Geol. 504, 38–52.
Kirkland, C., Fougerouse, D., Reddy, S., Hollis, J., Saxey, D., 2018. Assessing the mechanisms of common Pb incorporation into titanite. Chem. Geol. 483, 558–566.
Kirkland, C.L., Spaggiari, C.V., Johnson, T.E., Smithies, R.H., Danišík, M., Evans, N., Wingate, M.T.D., Clark, C., Spencer, C., Mikucki, E., McDonald, B.J., 2016. Grain size matters: implications for element and isotopic mobility in titanite. Precambrian Res. 278, 283–302.
Klötzli, U.S., Sinigoi, S., Quick, J.E., Demarchi, G., Tassinari, C.C., Sato, K., Günes, Z., 2014. Duration of igneous activity in the Sesia Magmatic System and implications for high-temperature metamorphism in the Ivrea–Verbano deep crust. Lithos 206, 19–33.
Kohn, M.J., 2017. Titanite petrochronology. Rev. Mineral. Geochem. 83, 419–441.
Kohn, M.J., Corrie, S.L., 2011. Preserved Zr-temperatures and U–Pb ages in high-grade metamorphic titanite: evidence for a static hot channel in the Himalayan orogen. Earth Planet. Sci. Lett. 311 (1–2), 136–143.
Köppel, V., 1974. Isotopic U–Pb ages of monazites and zircons from the crust-mantle transition and adjacent units of the Ivrea and Ceneri Zones (Southern Alps, Italy). Contrib. Mineral. Petrol. 43 (1), 55–70.
Kunz, B.E., Johnson, T.E., White, R.W., Redler, C., 2014. Partial melting of metabasic rocks in Val Strona di Omegna, Ivrea Zone, Northern Italy. Lithos 190–191, 1–12.
Kunz, B.E., Regis, D., Engi, M., 2018. Zircon ages in granulite facies rocks: decoupling from geochemistry above 850 °C? Contrib. Mineral. Petrol. 173, 1–21.
Kusiak, M.A., Kovaleva, E., Wirth, R., Klötzli, U., Dunkley, D.J., Yi, K., Lee, S., 2019. Lead oxide nanospheres in seismically deformed zircon grains. Geochim. Cosmochim. Acta 262, 20–30.
Langone, A., José, A.P.N., Ji, W.Q., Zanetti, A., Mazzucchelli, M., Tiepolo, M., Giovanardi, T., Bonazzi, M., 2017. Ductile–brittle deformation effects on crystal-chemistry and U–Pb ages of magmatic and metasomatic zircons from a dyke of the Finero Mafic Complex (Ivrea–Verbano Zone, Italian Alps). Lithos 284, 493–511.
Langone, A., Zanetti, A., Daczko, N.R., Piazolo, S., Tiepolo, M., Mazzucchelli, M., 2018. Zircon U–Pb dating of a lower crustal shear zone: a case study from the northern sector of the Ivrea-Verbano Zone (Val Cannobina, Italy). Tectonics 37, 322–342.
Locmelis, M., Fiorentini, M.L., Rushmer, T., Arevalo, R., Adam, J., Denyszyn, S.W., 2016. Sulfur and metal fertilization of the lower continental crust. Lithos 244, 74–93.
Lund, M.D., Piazolo, S., Harley, S.L., 2006. Ultrahigh temperature deformation microstructures in felsic granulites of the Napier Complex, Antarctica. Tectonophysics 427 (1–4), 133–151.
Manatschal, G., Müntener, O., Lavier, L.L., Minshull, T.A., Péron-Pinvidic, G., 2007. Observations from the Alpine Tethys and Iberia–Newfoundland margins pertinent to the interpretation of continental breakup. Geol. Soc. Spec. Publ. 282, 291–324.
McDonough, W.F., Sun, S.S., 1995. The composition of the Earth. Chem. Geol. 120 (3–4), 223–253.
McGregor, M., Erickson, T.M., Spray, J.G., Whitehouse, M.J., 2021. High-resolution EBSD and SIMS U–Pb geochronology of zircon, titanite, and apatite: insights from the Lac La Moinerie impact structure, Canada. Contrib. Mineral. Petrol. 176 (10), 1–25.
Moore, J., Beinlich, A., Porter, J.K., Talavera, C., Berndt, J., Piazolo, S., Austrheim, H., Putnis, A., 2020. Microstructurally controlled trace element (Zr, U–Pb) concentrations in metamorphic rutile: an example from the amphibolites of the Bergen Arcs. J. Metamorph. Geol. 38 (1), 103–127.
Moser, A.C., Hacker, B.R., Gehrels, G.E., Seward, G.G., Kylander-Clark, A.R., Garber, J.M., 2022. Linking titanite U–Pb dates to coupled deformation and dissolution–reprecipitation. Contrib. Mineral. Petrol. 177 (3), 1–27.
Mottram, C.M., Cottle, J.M., Kylander-Clark, A.R., 2019. Campaign-style U–Pb titanite petrochronology: along-strike variations in timing of metamorphism in the Himalayan metamorphic core. Geosci. Front. 10 (3), 827–847.
Mulch, A., Cosca, M., Handy, M., 2002. In-situ UV-laser 40 Ar/39 Ar geochronology of a micaceous mylonite: an example of defect-enhanced argon loss. Contrib. Mineral. Petrol. 142 (6), 738–752.
Oberti, R., Smith, D.C., Rossi, G., Caucia, F., 1981. The crystal-chemistry of high-aluminium titanites. Eur. J. Mineral., 777–792.
Papapavlou, K., Darling, J.R., Moser, D.E., Barker, I.R., White, L.F., Lightfoot, P.C., Dunlop, J., 2018. U–Pb isotopic dating of titanite microstructures: potential implications for the chronology and identification of large impact structures. Contrib. Mineral. Petrol. 173 (10), 1–15.
Peressini, G., Quick, J.E., Sinigoi, S., Hofmann, A.W., Fanning, M., 2007. Duration of a large mafic intrusion and heat transfer in the lower crust: a SHRIMP U–Pb Zircon study in the Ivrea-Verbano Zone (Western Alps, Italy). J. Petrol. 48, 1185–1218.
Petri, B., Duretz, T., Mohn, G., Schmalholz, S.M., Karner, G.D., Muntener, O., 2019. Thinning mechanisms of heterogeneous continental lithosphere. Earth Planet. Sci. Lett. 512, 147–162.
Piazolo, S., Austrheim, H., Whitehouse, M., 2012. Brittle-ductile microfabrics in naturally deformed zircon: deformation mechanisms and consequences for U–Pb dating. Am. Mineral. 97 (10), 1544–1563.
Piazolo, S., La Fontaine, A., Trimby, P., Harley, S., Yang, L., Armstrong, R., Cairney, J.M., 2016. Deformation-induced trace element redistribution in zircon revealed using atom probe tomography. Nat. Commun. 7 (1), 1–7.
Putnis, A., 2009. Mineral replacement reactions. Rev. Mineral. Geochem. 70, 87–124.
Putnis, A., Austrheim, H., 2010. Fluid-induced processes: metasomatism and metamorphism. Geofluids 10 (1–2), 254–269.
Redler, C., Johnson, T.E., White, R.W., Kunz, B.E., 2012. Phase equilibrium constraints on a deep crustal metamorphic field gradient: metapelitic rocks from the Ivrea Zone (NW Italy): Ivrea Zone metamorphic field gradient. J. Metamorph. Geol. 30, 235–254.
Rubatto, D., Hermann, J., 2003. Zircon formation during fluid circulation in eclogites (Monviso, Western Alps): implications for Zr and Hf budget in subduction zones. Geochim. Cosmochim. Acta 67, 2173–2187.
Rutter, E., Brodie, K., James, T., Burlini, L., 2007. Large-scale folding in the upper part of the Ivrea-Verbano zone, NW Italy. J. Struct. Geol. 29, 1–17.
Satsukawa, T., Piazolo, S., González-Jiménez, J.M., Colás, V., Griffin, W.L., O'Reilly, S.Y., Kerestedjian, T.N., 2015. Fluid-present deformation aids chemical modification of chromite: Insights from chromites from Golyamo Kamenyane, SE Bulgaria. Lithos 228, 78–89.
Scibiorski, E., Kirkland, C.L.C., Kemp, A.I.S., Tohver, E., Evans, N.J., 2019. Trace elements in titanite: a potential tool to constrain polygenetic growth processes and timing. Chem. Geol. 509, 1–19.
Scibiorski, E.A., Cawood, P.A., 2022. Titanite as a petrogenetic indicator. Terra Nova.
Scott, D.J., St-Onge, M.R., 1995. Constraints on Pb closure temperature in titanite based on rocks from the Ungava orogen, Canada: implications for U–Pb geochronology and PTt path determinations. Geology 23 (12), 1123–1126.
Simonetti, M., Langone, A., Corvò, S., Bonazzi, M., 2021. Triassic-Jurassic rift-related deformation and temperature-time evolution of the fossil Adriatic margin: a review from Ossola and Strona di Omegna valleys (Ivrea-Verbano Zone). Ofioliti 46 (2), 147–161.
Simonetti, M., Langone, A., Bonazzi, M., Corvò, S., Maino, M., 2023. Tectono-metamorphic evolution of a post-variscan mid-crustal shear zone in relation to the Tethyan rifting (Ivrea-Verbano Zone, Southern Alps). J. Struct. Geol. 104896.

Smye, A.J., Marsh, J.H., Vermeesch, P., Garber, J.M., Stockli, D.F., 2018. Applications and limitations of U–Pb thermochronology to middle and lower crustal thermal histories. Chem. Geol. 494, 1–18.

Spear, F.S., 1993. Metamorphic Phase Equilibria and Pressure-Temperature-Time Paths. Mineralogical Society of America Monograph, pp. 352–356.

Spencer, K.J., Hacker, B.R., Kylander-Clark, A.R.C., Andersen, T.B., Cottle, J.M., Stearns, M.A., Poletti, J.E., Seward, G.G.E., 2013. Campaign-style titanite U–Pb dating by laser ablation ICP: implications for crustal flow, phase transformations and titanite closure. Chem. Geol. 341, 84e101.

Spruzeniece, L., Piazolo, S., Maynard-Casely, H.E., 2017. Deformation-resembling microstructure created by fluid-mediated dissolution–precipitation reactions. Nat. Commun. 8 (1), 1–9.

Stearns, M.A., Hacker, B.R., Ratschbacher, L., Rutte, D., Kylander-Clark, A.R.C., 2015. Titanite petrochronology of the Pamir gneiss domes: implications for middle to deep crust exhumation and titanite closure to Pb and Zr diffusion. Tectonics 34 (4), 784–802.

Timms, N.E., Pearce, M.A., Erickson, T.M., Cavosie, A.J., Rae, A.S., Wheeler, J., Wittmann, A., Ferrière, L., Poelchau, M.H., Tomioka, N., Collins, G.S., Gulick, P.S., Rasmussen, C., Morgan, J.V., 2019. New shock microstructures in titanite (CaTiSiO5) from the peak ring of the Chicxulub impact structure, Mexico. Contrib. Mineral. Petrol. 174 (5), 1–23.

Varga, J., Raimondo, T., Daczko, N.R., Adam, J., 2020. Experimental alteration of monazite in granitic melt: variable U–Th–Pb and REE mobility during melt-mediated coupled dissolution-precipitation. Chem. Geol. 544, 119602.

Vavra, G., Schmid, R., Gebauer, D., 1999. Internal morphology, habit and U-Th-Pb microanalysis of amphibolite-to-granulite facies zircons: geochronology of the Ivrea Zone (Southern Alps). Contrib. Mineral. Petrol. 134, 380–404.

Walters, J.B., Cruz-Uribe, A.M., Song, W.J., Gerbi, C., Biela, K., 2022. Strengths and limitations of in situ U–Pb titanite petrochronology in polymetamorphic rocks: an example from western Maine, USA. J. Metamorph. Geol. 40 (6), 1043–1066.

Whitney, D.L., Evans, B.W., 2010. Abbreviations for names of rock-forming minerals. Am. Mineral. 95 (1), 185–187.

Williams, M.A., Kelsey, D.E., Rubatto, D., 2022. Thorium zoning in monazite: a case study from the Ivrea–Verbano zone, NW Italy. J. Metamorph. Geol. 40 (6), 1015–1042.

Wolff, R., Dunkl, I., Kiesselbach, G., Wemmer, K., Siegesmund, S., 2012. Thermochronological constraints on the multiphase exhumation history of the Ivrea-Verbano Zone of the Southern Alps. Tectonophysics 579, 104–117.

Zanetti, A., Mazzucchelli, M., Sinigoi, S., Giovanardi, T., Peressini, G., Fanning, M., 2013. SHRIMP U–Pb zircon Triassic intrusion age of the Finero mafic complex (Ivrea–Verbano Zone, Western Alps) and its geodynamic implications. J. Petrol. 54 (11), 2235–2265.

Zingg, A., 1990. The Ivrea crustal cross-section (Northern Italy and Southern Switzerland). In: Salisbury, M.H., Fountain, D.M. (Eds.), Exposed Cross-Sections of the Continental Crust. Springer Netherlands, Dordrecht, pp. 1–19.